Global biome patterns of the Middle and Late Pleistocene

Huntley, B. ORCID: https://orcid.org/0000-0002-3926-2257, Allen, J. R. M., Forrest, M., Hickler, T., Ohlemüller, R. ORCID: https://orcid.org/0000-0001-9102-6481, Singarayer, J. S. and Valdes, P. J. (2023) Global biome patterns of the Middle and Late Pleistocene. Journal of Biogeography, 50 (8). pp. 1352-1372. ISSN 1365-2699 doi: https://doi.org/10.1111/jbi.14619 Available at https://centaur.reading.ac.uk/112137/

Received: 30 November 2022 | Revised: 20 February 2023 | Accepted: 3 March 2023

DOI: 10.1111/jbi.14619

Journal of Biogeography

WILEY

SYNTHESIS

Global biome patterns of the Middle and Late Pleistocene

Brian Huntley[1] | Judy R. M. Allen[1] | Matthew Forrest[2] | Thomas Hickler[2,3] | Ralf Ohlemüller[4] | Joy S. Singarayer[5] | Paul J. Valdes[6]

[1]Department of Biosciences, Durham University, South Road, Durham, DH1 3LE, UK

[2]Senckenberg Biodiversity and Climate Research Centre, Senckenberganlage 25, D-60325, Frankfurt am Main, Germany

[3]Institute of Physical Geography, Goethe-University, Altenhöferallee 1, D-60438, Frankfurt am Main, Germany

[4]School of Geography, University of Otago, PO Box 56, Dunedin, 9054, New Zealand

[5]Department of Meteorology, University of Reading, PO Box 243, Reading, RG6 6BB, UK

[6]School of Geographical Sciences, University of Bristol, University Road, Clifton, Bristol, BS8 1SS, UK

Correspondence
Brian Huntley, Department of Biosciences, Durham University, South Road, Durham, DH1 3LE, UK; Boreland Lodge, Kirkcowan, Newton Stewart DG8 0DD, UK.
Email: brian.huntley@durham.ac.uk

Funding information
Leverhulme Trust

Handling Editor: Simon Scheiter

Abstract

Our primary aim was to assess the hypothesis that distinctive features of the patterns of vegetation change during successive Quaternary glacial–interglacial cycles reflect climatic differences arising from forcing differences. We addressed this hypothesis using 207 half-degree resolution global biome pattern simulations, for time slices between 800 and 2 ka, made using the LPJ-GUESS dynamic global vegetation model. Simulations were driven using ice-core atmospheric CO_2 concentrations, Earth's obliquity, and outputs from a pre-industrial and 206 palaeoclimate experiments; four additional simulations were driven using projected future CO_2 concentrations. Climate experiments were run using HadCM3. Using a rule-based approach, above-ground biomass and leaf area index of LPJ-GUESS plant functional types were used to infer each grid cell's biome. The hypothesis is supported by the palaeobiome simulations. To enable comparisons with the climatic forcing, multivariate analyses were performed of global vegetation pattern dissimilarities between simulations. Results showed generally similar responses to glacial–interglacial climatic variations during each cycle, although no two interglacials or glacials had identical biome patterns. Atmospheric CO_2 concentration was the strongest driver of the dissimilarity patterns. Dissimilarities relative to the time slice with the lowest atmospheric CO_2 concentration show the log-linear relationship to atmospheric CO_2 concentration expected of an index of ecocarbon sensitivity. For each simulation, extent and total above-ground biomass of each biome were calculated globally and for three longitudinal segments corresponding to the major continental regions. Mean and minimum past extents of forest biomes, notably Temperate Summergreen Forest, in the three major continental regions strongly parallel relative tree diversities, hence supporting the hypothesis that past biome extents played an important role in determining present diversity. Albeit that they reflect the climatic consequences only of the faster Earth system components, simulated potential future biome patterns are unlike any during the past 800 ky, and likely will continue to change markedly for millennia if projected CO_2 concentrations are realised.

KEYWORDS
above-ground plant biomass, atmospheric CO_2 concentration, ecocarbon sensitivity, glacial–interglacial cycle, HadCM3, leaf area index, LPJ-GUESS, multivariate analysis, palaeovegetation maps, RCP4.5 and RCP8.5

1 | INTRODUCTION

The Middle and Late Pleistocene, the last 780ky (Gibbard et al., 2005), is characterised by alternating glacial and interglacial stages, with glacial terminations (rapid transitions from glacial to interglacial conditions) occurring at ca. 100ky intervals. Hays et al. (1976), using stable oxygen isotopes from marine microfossils, demonstrated that these climatic fluctuations were driven by variations in the Earth's orbit (Milankovitch cycles). Given that the orbital forcing of climate during each glacial–interglacial cycle was unique, so too were the resulting climatic conditions as recorded by various palaeoclimatic proxies (Figure S1). Palaeovegetation records spanning two or more glacial–interglacial cycles, although sparsely distributed globally, similarly evidence vegetation differences, especially between successive interglacials, at any one location (e.g. Miyoshi et al., 1999; Tzedakis, 1994). In Europe, which has the highest density of such records, these also evidence the unique temporal development of vegetation across the continent during different interglacial stages. For more than three decades, the generally accepted hypothesis has been that the unique vegetation characteristics of each glacial–interglacial cycle resulted from climatic differences, and that these, in turn, resulted from differences in orbital forcing and their effects on, for example, ice-sheet extent and albedo, as well as on atmospheric concentrations of naturally occurring greenhouse gases (carbon dioxide, methane and nitrous oxide). As Watts (1988) wrote, '*each well-studied interglacial period reveals a coherent and protracted development of vegetation in response to climatic change*' (p. 160), the diversity of expression of interglacials being '*most probably a response to the interrelation of the three main orbital parameters which may result in distinctive forcing patterns and seasonality for each separate interglacial*' (p. 161).

Despite its paradigm status, there are several reasons why this hypothesis, that the differing spatiotemporal vegetation patterns of different interglacials reflect differing climatic patterns as a consequence of novel orbital forcing, has not to-date been systematically tested. The principal problem is obtaining independent continental palaeoclimatic records for successive glacial–interglacial cycles with which objectively to compare palaeovegetation records. Although pollen records can be used to infer palaeoclimate (e.g. Allen & Huntley, 2009; Newnham et al., 2017), this leads to circularity of argument if the inferred palaeoclimate is subsequently compared with the palaeovegetation evidence. An alternative approach, applied to the period since the last glacial maximum (LGM), is to simulate palaeoclimate using a general circulation model (GCM) and compare the simulated climate with the palaeovegetation evidence. Comparison may be achieved either by driving a vegetation model using the simulated climate and comparing the simulated vegetation with that recorded by pollen data (see e.g. Bigelow et al., 2003; Kaplan et al., 2003), or by quantitatively reconstructing palaeoclimate from palaeovegetation data and comparing the results with the GCM-simulated climate (e.g. Harrison et al., 2014). Whilst both approaches have been applied successfully to a number of regions, and to the period since the LGM, their utility is limited in regions where, or during times when, palaeovegetation records are sparse. Both are also difficult to apply to intervals beyond ca. 50ka, the effective limit of ^{14}C (radiocarbon) dating, without a potential for circularity if palaeovegetation records are dated by 'tuning' to marine oxygen isotope (MOI) records of ice volume and/or to orbital forcing (see e.g. Torres et al., 2013).

Effective application of either data–model comparison approach also requires a large number of palaeovegetation data points. Palaeovegetation records spanning two or more glacial–interglacial cycles at a single locality, however, are globally extremely sparse in occurrence. Although a larger number of records, each representing a single interglacial stage, is available, independently dating such records is even more difficult than is dating records spanning two or more glacial–interglacial cycles. This is well illustrated by the historical recognition in Europe of only two Middle/Late Pleistocene interglacials, referred to as the Eemian (last) and Holsteinian (penultimate). For many decades, all records, most spanning only a single interglacial or part of an interglacial, were assigned to whichever of the Eemian or Holsteinian their palaeovegetation sequence showed greater similarity (see e.g. Hall, 1980). When records were obtained spanning two or more glacial–interglacial cycles, however, these provided definitive evidence of two additional glacial–interglacial cycles interposed between the Holsteinian interglacial, as generally recognised, and the last interglacial (LIG), conventionally labelled the Eemian and correlated with MOI Sub-stage 5e. Key records in this context include that from the Ioanina basin, north-west Greece (Tzedakis, 1994), extending continuously back to MOI Stage 12, the overlapping records from the Velay, Massif Central, France, each spanning two or three interglacial stages (Reille et al., 2000), and independently dated records from various sites in England (Penkman et al., 2011; Schreve, 2001, 2019). The Holsteinian thus corresponds to MOI Stage 11, and a number of interglacial records from Europe formerly assigned to either the Holsteinian or the Eemian are now recognised as representing MOI Stages 9 or 7. Despite these advances, independently assigning an age to a record from Europe representing a single interglacial stage remains difficult (Tzedakis et al., 2001). Elsewhere in the world it is often virtually impossible, unless, for example, tephra layers are present in the sediment sequence containing the interglacial deposits and can be dated independently (e.g. Westgate & Pearce, 2017), or the record can be correlated unambiguously with a long continuous palaeovegetation record (e.g. Kershaw et al., 2007; Litwin et al., 1997; Singh et al., 1985; Torres et al., 2013), which is rarely achievable.

Notwithstanding these difficulties, our initial objective was to assess whether and how global vegetation patterns, and their temporal development, differed between successive Middle and Late Pleistocene glacial–interglacial cycles, and whether any differences related to differences in climatic boundary conditions, and hence climatic patterns, as the paradigm hypothesis proposes. Given that the sparse palaeovegetation data preclude a temporally and spatially comprehensive synthesis of global palaeovegetation patterns, even for the most recent glacial–interglacial cycle, and given also the dating and other difficulties described above, we adopted

a modelling approach. The LPJ-GUESS dynamic global vegetation model (DGVM; Smith et al., 2001, 2014) was used to simulate global vegetation characteristics for a series of time slices for which GCM simulations of palaeoclimate were available. LPJ-GUESS outputs were then used to infer global biome patterns. Simulations were made for the 'present' and for 206 past time slices between 800 and 2 ka, thus spanning the nine glacial–interglacial cycles commencing with MOI Stage 20. Ten intervals with interglacial characteristics are represented (MOI Stages/Sub-stages 19, 17, 15e, 15a, 13, 11, 9e, 7e, 5e and 1), as are nine intervals with global ice volume indicating substantial glaciation, albeit not always as extensive as at the LGM (MOI Stages 2, 6, 8, 10, 12, 14, 16, 18 and 20). In addition, substantial periods of intermediate ice volume, including a number of interstadials (e.g. MOI sub-stages 3, 5a, 5c and 9a), are represented. Mapping and analysis of the simulation results enabled assessment of the nature of global biome patterns, and their relationship to climatic boundary conditions, since 800 ka.

Given evidence from the simulations of the changing extent and location of biomes since 800 ka, we also explored the extent to which past variations in extent of biomes on the principal continental regions may account for present diversity patterns of key organism groups in those biomes, as argued by Huntley (1993) for northern hemisphere temperate forests. By performing equivalent simulations of potential global biome patterns for projected future climatic conditions and atmospheric carbon dioxide concentration ($[CO_2]_{atm}$), we also explored the extent to which future patterns may differ from any since 800 ka.

2 | MATERIALS AND METHODS

2.1 | Climate experiments

An internally consistent series of 206 palaeoclimate experiments, plus a 'pre-industrial' experiment (using mid-twentieth century ice-sheet and orbital boundary conditions, but pre-industrial [ca. 1800 CE] atmospheric concentrations of CO_2, CH_4 and N_2O, see 0 ka experiment, Table S1), as well as four experiments representing potential future conditions in 2050 and 2100 under the RCP4.5 and RCP8.5 pathways (van Vuuren et al., 2011), were performed using the HadCM3 fully coupled atmosphere–ocean general circulation model (AOGCM). Design of the experiments followed Singarayer and Valdes (2010) with respect to the boundary conditions and forcings applied (Table S1), but with two important exceptions. First, rather than using a static pre-industrial land surface for all experiments, the AOGCM was coupled to Triffid (Cox, 2001), a simple DGVM with five plant functional types (PFTs), enabling vegetation structure and associated climatically important land-surface properties to interact dynamically with the atmosphere. Second, ice sheets were specified following de Boer et al. (2013, 2014) who modelled the history of the four major global ice sheets (Antarctic, Eurasian, Greenland and North American) over the past 5 My, providing simulated extents and thicknesses for each at 2 ky intervals (de Boer, 2014). Simulations were run for a minimum of 500 years to obtain a climate in quasi-equilibrium with the imposed boundary conditions. Simulations did not include millennial scale forcing (e.g. meltwater pulses) and hence do not include Heinrich and Dansgaard-Oeschger events. The precise model configuration is HadCM3B-M2.1aD, as defined by Valdes et al. (2017) who showed that this configuration of the model outperforms many higher-fidelity CMIP5 models. More details of model setup can be found in Davies-Barnard et al. (2017).

For each palaeoclimate and potential future experiment, anomalies relative to the pre-industrial experiment were calculated for monthly mean temperatures (°C), monthly precipitation totals (mm) and monthly mean cloudiness (% potential bright sunshine). Anomalies were calculated using the climatology of the last 100 years of the experiment in each case and interpolated to the centres of the cells of the 0.5 × 0.5° grid used with LPJ-GUESS.

2.2 | LPJ-GUESS simulations

Following Huntley et al. (2013), the potential 1901–1930 annual time series of monthly mean temperature, monthly precipitation and monthly mean cloudiness for 0.5 × 0.5° grid cells on shelf areas exposed by lowered glacial sea levels were estimated using thin-plate spline surfaces fitted to data for the 0.5 × 0.5° land grid cells in the CRU TS 3.0 dataset (Harris et al., 2014). Following the approach of Miller et al. (2008), anomalies derived from the palaeoclimate and potential future experiments were applied to the 1901–1930 annual time series of climatic data for each CRU TS 3.0 land grid cell and each shelf grid cell, monthly mean temperature time series first being detrended to remove the warming trend over those three decades. Atmospheric carbon dioxide concentration for each past time slice was determined according to Antarctic ice-core data (Loulergue et al., 2008; Lüthi et al., 2008; Petit et al., 1999) using the EDC3 chronology (Parrenin et al., 2007). Obliquity was specified following Laskar et al. (2004). Boundary conditions for potential future simulations were specified as in Huntley et al. (2021). Soil textures were specified for all time slices using present-day values (Haxeltine & Prentice, 1996), shelf cells being specified as having a medium-coarse soil texture.

LPJ-GUESS simulations were performed as described by Allen et al. (2020) using the carbon-only version of the model (Smith et al., 2014). In all, 20 PFTs were used, comprising 11 tree, 7 shrub and 2 grass PFTs, attributes of which were defined by Allen et al. (2020). In total, 25 replicate 0.1 ha stands, a number more than sufficient to achieve a relatively stable 'equilibrium' PFT composition (Smith et al., 2001), were simulated for each 0.5 × 0.5° grid cell. The model was spun-up from bare ground for 500 simulated years, a sufficient period for the simulated vegetation to reach approximate equilibrium with the climate and $[CO_2]_{atm}$ (Hickler et al., 2012), and then run for a further 90 simulated years. The 30-year climatic time series for the grid cell was cycled through repeatedly as required. Grid cell values of vegetation attributes were computed as the overall mean of the mean simulated values

for the final 90 years for the 25 replicate stands. Simulations were run for 206 time slices for which palaeoclimate experiment results were available, as well as for the 'present' and four RCP scenarios. For the 'present' simulation, 1901–1930 climatic data were used without applying anomalies but with detrended monthly temperatures, atmospheric carbon dioxide concentration was 280 ppmv and obliquity specified at its contemporary value. Two variables computed by LPJ-GUESS for each PFT were used to infer biome type for each grid cell at each time slice: cmass—above-ground vascular plant biomass (referred to hereafter as carbon mass); and lai—leaf area index (LAI). Grid cell total carbon mass for each PFT, and overall, was computed using estimated ice-free land area of the grid cell at that time (see Appendix S1).

2.3 | Biome inference

The biome occupying each 0.5° grid cell during each time slice was inferred from simulated LAI and carbon mass values for the 20 PFTs using the rule-based procedure described by Allen et al. (2020). In all, 21 biomes were recognised (Table S2), the small minority of grid cells not matching the criteria for any biome being categorised as Unclassified. Global biome distributions were mapped for all time slices using ArcMap 10.5®, ice-sheet and ocean masks being overlain onto each map, and the maps compiled as a slideshow (see Supporting Information, Slideshow). The following measures were calculated for each time slice, globally and for three longitudinal segments (135° W–30° W—Americas; 30° W–65° E—Europe–Africa; and 65° E–135° W—Asia–Beringia): extent of each biome, both as total area (10^3 km^2) and as percentage of ice-free land area; number and percentage of grid cells with ice-free land assigned to each biome; total carbon mass (kg) for each biome; total ice-free land area; number of grid cells with ice-free land; and overall total carbon mass. For each biome, global total carbon mass of each PFT and percentage of the biome's total carbon mass contributed by each PFT were also calculated for each time slice.

2.4 | Multivariate analyses

To quantify differences between biome patterns for pairs of time slices, a measure of dissimilarity was first calculated for each grid cell. This was computed as the sum of two components, the first reflecting the difference in bioclimatic zone, according to the simulated vegetation, and the second the difference in vegetation structure. Each biome was assigned to one, or in two cases two, of six bioclimatic zones, and to one, or in one case two, structural types (Table S2). Dissimilarity between adjacent bioclimatic zones was defined as 20 units, dissimilarities between non-adjacent zones being appropriate multiples of 20 units (Table S3). For structural types, dissimilarities used a non-linear scaling designed to emphasise the greater magnitude of structural difference between forest and non-forest biomes, and also to assign a small dissimilarity even when two biomes' structural types were the same, thus avoiding zero dissimilarity between biomes of the same structural type in the same bioclimatic zone (Table S4). Because the Desert biome encompasses both polar and warm temperate/sub-tropical deserts, when computing the matrix of dissimilarities between biomes (Table S5), dissimilarities between Desert and other biomes were calculated after first assigning the Desert biome either to the Arctic or to the Warm temperate/Sub-tropical bioclimatic zone, whichever was closer to the bioclimatic zone of the biome with which it was being compared. Semi-desert biome dissimilarities were calculated as the mean of two values taking its structural type as Grassland and as Shrubland, this biome being intermediate between these structural types. Similarly, Temperate Broadleaved Evergreen Forest biome dissimilarities were calculated as the mean of two values taking its bioclimatic zone as Temperate and as Warm temperate/Sub-tropical, this biome spanning these bioclimatic zones.

Using the dissimilarity matrix between biomes, grid-cell dissimilarities between the biomes occupying each grid cell for each of a pair of time slices were assigned for all grid cells with non-zero ice-free land area for both time slices being compared, excluding grid cells for which the biome was Unclassified. The global weighted mean, weights being the ice-free land areas of the grid cells, of these grid-cell dissimilarity values was then used as the overall dissimilarity between global biome patterns for the two time slices. Dissimilarity values were computed in this way for all possible time-slice pairs and the resulting dissimilarity matrix used as input to the multivariate analyses.

To enable comparison with the dissimilarities in biome patterns, dissimilarities in climatic forcing between time slices were computed as the standardised Euclidean Distance using three forcing factors: northern hemisphere summer insolation, using the value for the month June 21st to July 20th at 65° N, computed following Laskar et al. (2004); global ice volume, as reflected by the LR04 Global Pliocene–Pleistocene Benthic δ^{18}O stack (Lisiecki & Raymo, 2005); and atmospheric carbon dioxide concentration, derived from Antarctic ice-core measurements (Bereiter et al., 2015; Lüthi et al., 2008, data downloaded from http://ncdc.noaa.gov/paleo/study/17975 [3 October 2019]). In addition, Paleontological Statistics V4.10 (PAST; Hammer et al., 2001) was used to perform a multiple linear regression with these three variables as independent variables and biome dissimilarity as the dependent variable.

The biome pattern dissimilarity matrix was also subjected to multivariate analysis, both ordination and classification methods being applied. Ordination was performed using both principal coordinates analysis (PCoord), as implemented in PAST, and non-metric multidimensional scaling (NMDS), using the 'metaMDS' function in the R-package 'vegan' Version 2.5-7 (R Core Team, 2021) The dataset was classified using *K*-means cluster analysis, a non-hierarchical method, as implemented in PAST.

3 | RESULTS

Overall, our inferred global biome pattern for 0 ka (Figure S2) matches well the potential global present vegetation pattern (e.g. Olson, 1992

as mapped by; Haxeltine & Prentice, 1996; Prentice et al., 1992). Similarly, there is a good overall match between our inferred global biome pattern at the LGM and biomes inferred from palynological data (e.g. Ciais et al., 2012; Prentice et al., 2011). Furthermore, LPJ-GUESS, in the variant that we use without a simulated nitrogen cycle, is generally somewhat less sensitive to changes in $[CO_2]_{atm}$ than many similar models, similarly somewhat under-estimating vegetation sensitivity compared to Free Air CO_2 Enrichment (FACE) experiment results (see Terrer et al., 2019, figure 3a). This low sensitivity to $[CO_2]_{atm}$, despite the standard Farquhar-based photosynthesis module, results from a strong co-limitation of photosynthesis by plant-root-available water if plants are water-stressed (Hickler et al., 2008). Given this evidence, our maps can be viewed as reasonably accurate representations of likely global biome patterns, even though we acknowledge that the simulated plant-physiological responses to $[CO_2]_{atm}$ changes are somewhat uncertain.

3.1 | Interglacial global biome patterns

Overall global biome patterns for the 10 time slices falling closest to ice-volume minima comparable to that of the Holocene, and thus representing interglacials (Figure S3), are broadly similar to the present potential biome pattern (Figure S2). However, closer inspection reveals that no two are identical, with many regional differences in biome patterns; four examples serve to illustrate the range of these variations (Figure 1). Notable amongst these are varying relative extents of Boreal Evergreen Needle-leaved Forest and Boreal Parkland in both Eurasia and North America. Boreal Evergreen Needle-leaved Forest is most extensive during MOI Stages/Sub-stages 1 (8.9 Mm^2), 15e (10.3 Mm^2) and 19 (9.5 Mm^2), and least extensive during 13 (5.1 Mm^2), 15a (5.8 Mm^2) and 17 (5.2 Mm^2), whereas Boreal Parkland is most extensive during 5e (12.2 Mm^2), 11 (11.7 Mm^2), 15a (13.3 Mm^2) and 17 (11.3 Mm^2) and least extensive during 1 (7.1 Mm^2), 15e (4.6 Mm^2) and 19 (5.4 Mm^2). Tropical Evergreen Forest extent in the Europe–Africa longitudinal segment ranges between 3.4 Mm^2 during MOI Stage 1 and 2.5 Mm^2 during MOI Sub-stage 15a, the latter value being only 69% of the former. In the Asia–Beringia segment, that includes Australasia, the extent of Desert varies very considerably between interglacials, reaching 5.3 Mm^2 during MOI Sub-stage 15e but only 1.1 Mm^2 during MOI Stage 11 and 1.3 Mm^2 during MOI Sub-stage 5e. In the Americas segment Temperate Summergreen Forest extent ranges between 1.4 Mm^2 during MOI Sub-stage 15e and 2.2 Mm^2 during each of MOI Stages 11 and 13, whereas Temperate Parkland has extents of only 0.57 Mm^2 during MOI Sub-stage 15e and 0.58 Mm^2 during MOI Stage 19, but extends to 1.9 Mm^2 during MOI Stage 17 and 2.0 Mm^2 during MOI Sub-stage 15a.

An exhaustive listing of further regional differences is not appropriate here, but their overall magnitudes are summarised by biome pattern dissimilarities between the 10 interglacials and the present (Table 1). These identify MOI Stage 17 and Sub-stage 15a as those having global biome patterns most different from that of the present and MOI Sub-stage 9e as that with a global biome pattern most similar to the present.

Examination of the complete series of global biome maps (Supporting Information, Slideshow) reveals further regional differences between interglacials with respect to simulated temporal patterns of biome changes. Such differences in temporal patterns between interglacials are consistent with evidence from those few locations providing records of two or more interglacial palaeovegetation sequences (e.g. Allen et al., 2002; Allen & Huntley, 2009; Miyoshi et al., 1999; Tzedakis, 1994).

3.2 | Glacial global biome patterns

Once again, overall global biome patterns are broadly similar for the time slices closest to the ice volume maxima of the last nine glacial stages (Figure S4). The 668 ka time slice, although falling well before the MOI Stage 16 ice volume maximum, shows a similar biome pattern and is included in Figure 2 and Figure S4 because it is the past time slice with greatest dissimilarity in biome pattern from the present. Common features, illustrated by the four examples shown in Figure 2, include extensive areas of cold Desert, Tundra and Shrub Tundra in north-eastern Eurasia, much reduced forest biome area in Europe and western Eurasia, considerably increased extents of Desert in Australia and Eurasia, a very limited extent of Boreal Evergreen Needle-leaved Forest in North America, a much reduced area of Tropical Raingreen Forest in Africa and a much increased extent of Savanna in south-east Asia, including areas of the Sunda Shelf exposed by the lowered glacial sea level. Nonetheless, as with the interglacials, there are also marked differences in biome patterns, especially regionally, between different glacial stages. In Europe, where Boreal Evergreen Needle-leaved Forest is very restricted and Boreal Parkland extensive only north of the Black Sea during MOI Stage 2, both are much more extensive during some earlier glacial stages, in some cases, notably MOI Stage 8 (Figure 2c), forming a more or less continuous belt from western Europe to the Far East. Boreal Evergreen Needle-leaved Forest extent in the Europe–Africa segment is only 0.28 Mm^2 during MOI Stage 2 and 0.25 Mm^2 during MOI Stage 12, but 2.1 Mm^2 during MOI Stage 10. Globally, Boreal Evergreen Needle-leaved Forest has an extent of only 2.1 Mm^2 during MOI Stages 2 and 12, but of 4.3 Mm^2 during MOI Stage 10, whilst Boreal Parkland has an extent of 3.0 Mm^2 during MOI Stage 6 but of 8.0 Mm^2 during MOI Stage 14. In the Asia–Beringia segment, Tundra ranges in extent between 2.0 Mm^2 during MOI Stages 8 and 14 and 4.2 Mm^2 during MOI Stage 2, whilst Shrub Tundra ranges between 4.6 Mm^2 during MOI Stage 14 and 7.7 Mm^2 during MOI Stage 6, but reaching 8.8 Mm^2 at 668 ka, during MOI Stage 16.

Amongst other global features consistent with palaeovegetation records (e.g. Marchant et al., 2009; Prentice et al., 2000, 2011), greater extents of grassland biomes, including Savanna, Tropical Grassland and Steppe, during glacial stages are notable. For interglacial time slices, mean and median extents of Savanna, Tropical Grassland and

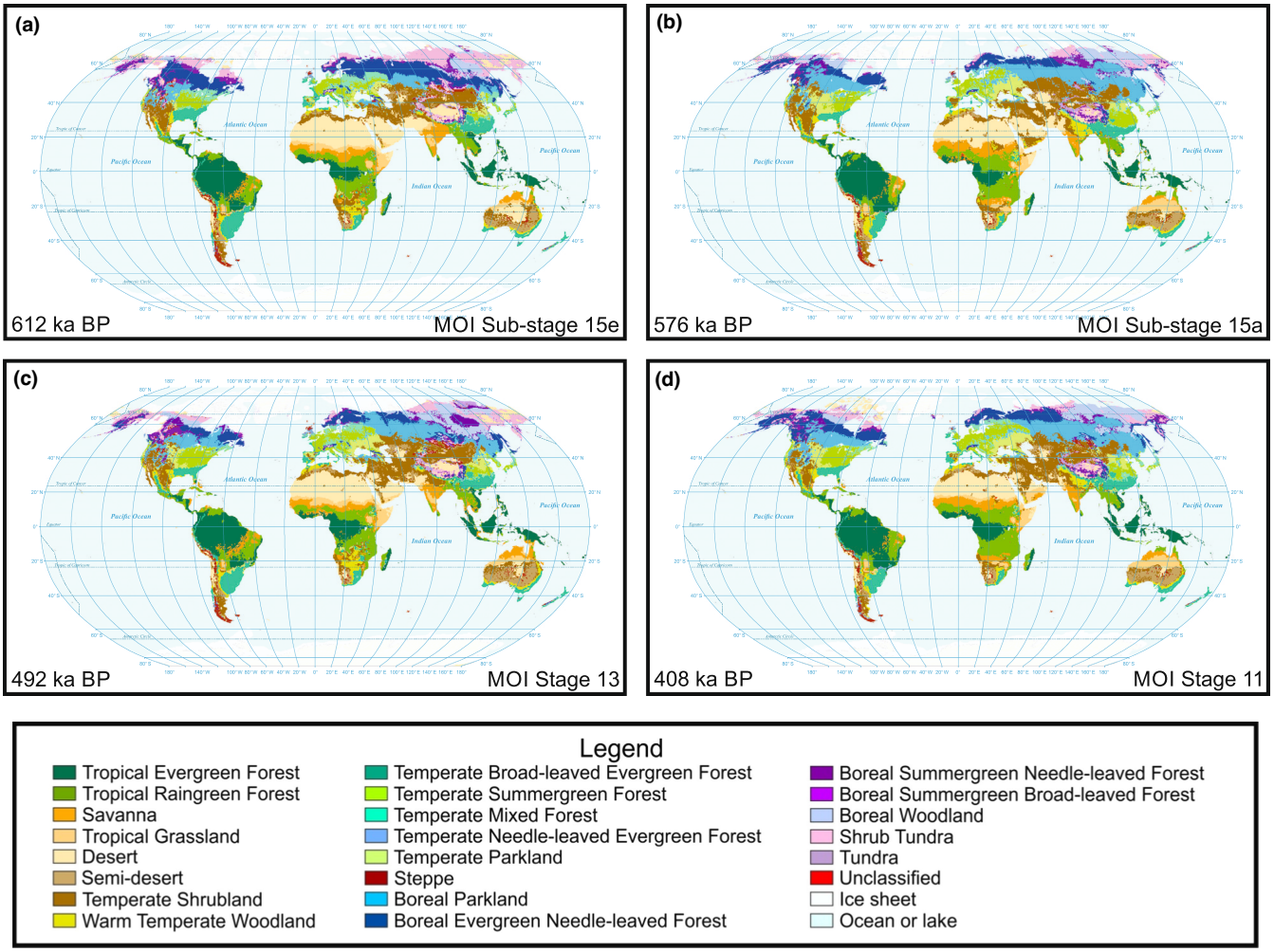

FIGURE 1 Simulated selected interglacial biome patterns. Inferred biomes are mapped for four selected marine oxygen isotope stages/sub-stages that approach or reach global ice volume minima similar to that of the Holocene, and that thus can be considered interglacials. Time slices shown are those closest in age to the ice-volume minimum of each marine oxygen isotope stage/sub-stage. The four marine oxygen isotope stages/sub-stages shown are selected to illustrate the range of variation in interglacial biome patterns. (Maps drawn using the Robinson Projection.)

TABLE 1 Interglacial stage global biome pattern dissimilarities.

Marine oxygen isotope stage/sub-stage	Palaeoclimate and biome age	Biome pattern dissimilarity with respect to 0 ka BP
1	2	1.666
5e	124	4.543
7e	240	4.551
9e	328	2.419
11	408	4.292
13	492	3.643
15a	576	5.643
15e	612	4.487
17	696	5.745
19	780	4.007

Note: See text for details of calculation of dissimilarity values.

Steppe are, respectively, 6.8 and 6.6 Mm^2, 4.7 and 4.6 Mm^2 and 1.8 and 1.8 Mm^2, whereas for glacial time slices their mean and median extents are, respectively, 8.7 and 9·0 Mm^2, 5.5 and 5.5 Mm^2 and 4.0 and 4.2 Mm^2. That Steppe shows the greatest contrast in simulated extent is also consistent with the palaeovegetation record, on the basis of which large parts of the temperate latitudes are inferred to have been occupied by Steppe during glacial times (see e.g. Prentice et al., 2011). Furthermore, the simulated LGM global biome pattern (MOI Stage 2, 18 ka, Figure 2d) has good visual matches to the maps of 'megabiomes' inferred from palynological data by Ciais et al. (2012 Figure S2) and of biomes inferred from the same data by Prentice et al. (2011).

Dissimilarities in biome patterns between glacial stages and the present, and between earlier glacial stages and MOI Stage 2 (Table 2), identify MOI Stage 14 as the least dissimilar from the present and MOI Stage 2 as the most dissimilar, apart from 668 ka BP which has the greatest dissimilarity from the present of all past time slices simulated, also being the time slice with the lowest $[CO_2]_{atm}$.

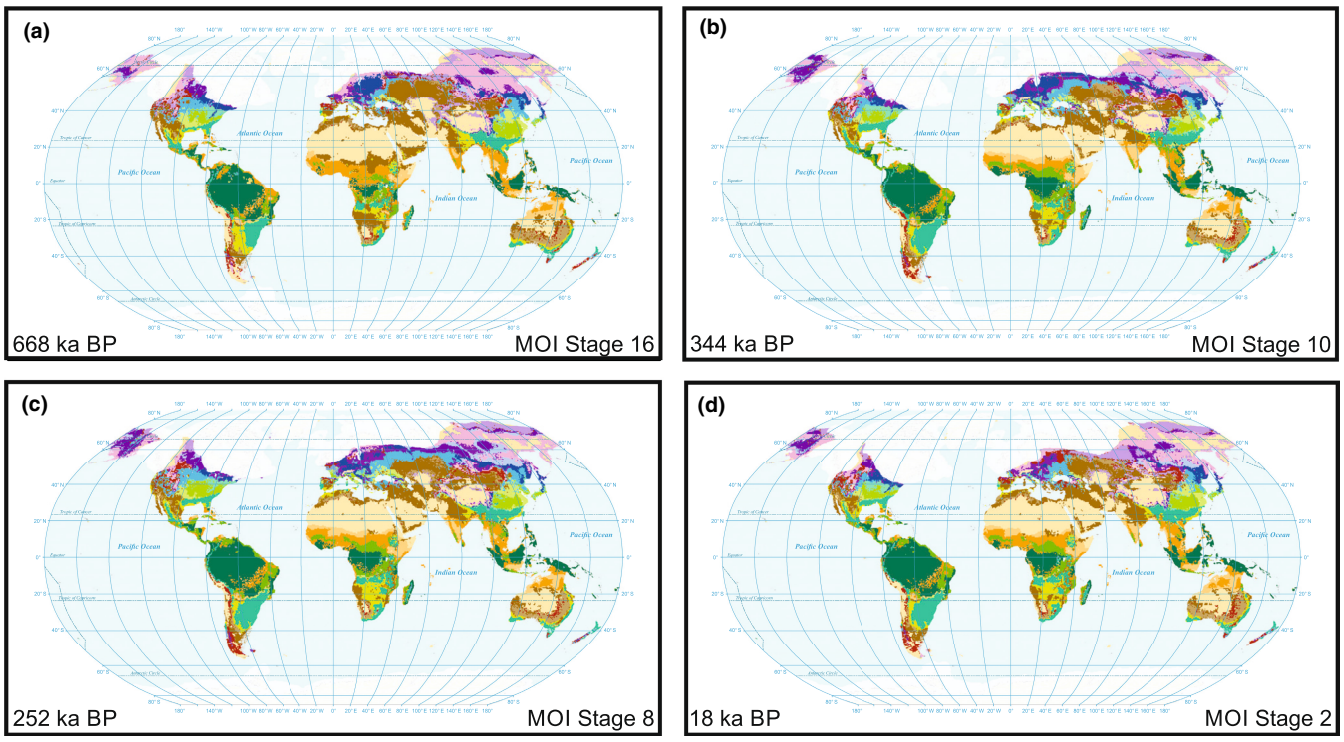

FIGURE 2 Simulated selected full glacial biome patterns. Inferred biomes are mapped for four selected marine oxygen isotope stages with global ice volume maxima similar in magnitude to that of the Last Glacial Maximum, and that thus can be considered fully glacial. With one exception, the time slices shown are those closest in age to the ice-volume maximum of each marine oxygen isotope stage. The exception is 668 ka that, although it falls within marine oxygen isotope Stage 16, is not the closest time slice to the ice volume maximum. However, the biome pattern for 668 ka has the greatest dissimilarity from the present biome pattern. (Maps drawn using the Robinson Projection. For Legend, see Figure 1.)

TABLE 2 Glacial stage global biome pattern dissimilarities.

Marine oxygen isotope stage	Palaeoclimate and biome age	Biome pattern dissimilarity with respect to	
		0 ka BP	18 ka BP
2	18	10.879	–
6	140	10.761	4.919
8	252	8.891	5.704
10	344	8.996	4.831
12	432	9.883	2.996
14	536	8.134	7.077
16	632	10.412	3.797
16[a]	668	12.526	5.851
18	720	9.994	4.159
20	796	10.276	3.490

Note: See text for details of calculation of dissimilarity values.
[a]Additional time slice included because it has the greatest dissimilarity from the present.

Of earlier glacial time slices, MOI Stage 12 is the least dissimilar, and MOI Stage 14 the most dissimilar, from MOI Stage 2.

As with the interglacials, examination of the complete series of global biome maps (Supporting Information, Slideshow) reveals further regional differences between glacials with respect to simulated temporal patterns of biome changes. Such differences in temporal patterns are again consistent with palaeovegetation evidence from those rare locations spanning two or more glacial stages.

3.3 | Overall history of global biome patterns 800 ka to present

Whilst careful visual examination of the maps of inferred past biome patterns (Supporting Information, Slideshow) can reveal many details of the changing simulated biome patterns since 800 ka, these temporal changes are usefully summarised by the dissimilarity value for each time slice with respect to the present (Figure 3). Furthermore, comparison of these dissimilarity values with standardised Euclidean Distance values, computed for each time slice relative to present in the space of the three principal climatic forcing factors (65° N summer insolation, global ice volume and atmospheric CO_2 concentration), reveals the two dissimilarity value series to be closely correlated (Figure 3). Linear regression of global biome pattern dissimilarities on standardised Euclidean Distances, the regression line being constrained to pass through the origin, confirmed a highly significant positive relationship ($F = 7398$, df 1206, $p = 0.8 \times 10^{-162}$, adjusted $R^2 = 0.968$), dissimilarity in global biome pattern being dependent on dissimilarity in principal climatic forcing factors.

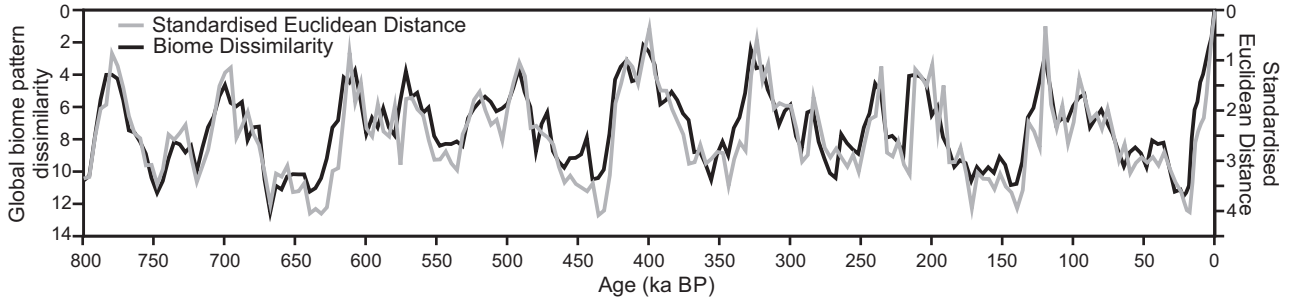

FIGURE 3 Global biome pattern and climatic forcing factor dissimilarity. Dissimilarity values between inferred past and present global biome patterns (black line), and standardised Euclidean Distance values relative to present (grey line) computed in the space of three climatic forcing factors: 65° N summer insolation (21 June–20 July; Laskar et al., 2004); global ice volume, as reflected by a global benthic $\delta^{18}O$ stack (Lisiecki & Raymo, 2005); and atmospheric CO_2 concentration (Bereiter et al., 2015), both dissimilarity value series being plotted against age for the 206 past time slices.

Relative contributions of the three climatic forcing factors to this pattern of dependence were investigated using multiple linear regression, with global biome pattern dissimilarity as dependent variable and the three forcing factors as independent variables. The results (Table 3) showed a highly significant relationship, identifying $[CO_2]_{atm}$ as the strongest individual predictor, followed by global ice volume. Summer insolation at 65° N had a much weaker relationship, although its p value of 0.00516 would still generally be considered to indicate a significant relationship. The strongest relationship with $[CO_2]_{atm}$ likely reflects that, in addition to affecting global climate, this has direct effects on aspects of plant physiology, notably photosynthesis, stomatal conductance and transpiration, that are simulated by LPJ-GUESS (e.g. Forrest et al., 2015; Hickler et al., 2008).

Ordinations of the global biome pattern dissimilarity matrix using PCoord and NMDS gave very similar results. The first two PCoord axes (Figure 4) together accounted for 59.5% of total variance, the third axis accounting for only a further 5.98%. First axis scores are strongly correlated positively with $[CO_2]_{atm}$ ($r=0.891$) and negatively with global ice volume ($r=-0.879$); correlation with 65° N summer insolation is positive but much weaker ($r=0.326$). Strongest correlation for second axis scores is with 65° N summer insolation ($r=0.577$), correlations for the other two variables being much weaker ($[CO_2]_{atm}$ $r=-0.287$; global ice volume $r=0.251$). NMDS analysis also gave a very good fit to the data, R^2 for the non-metric fit being 0.994 and the stress plot (Figure S5) showing an excellent fit between global biome pattern dissimilarities and distance in the ordination space. First axis scores are strongly correlated negatively with $[CO_2]_{atm}$ ($r=-0.877$) and positively with global ice volume ($r=0.877$); correlation with 65° N summer insolation is also negative but much weaker ($r=-0.348$). The NMDS first axis is thus essentially a reflection of the PCoord first axis. The second NMDS axis parallels the second PCoord axis, having its strongest (positive) correlation with 65° N summer insolation ($r=0.568$), and weaker correlations with the other variables ($[CO_2]_{atm}$ $r=-0.317$; global ice volume $r=0.271$). The plot of first and second NMDS axis scores (Figure S6) is thus very close to a horizontal mirroring of the plot of PCoord first and second axis scores (Figure 4).

Examination of the *K*-means cluster analysis results showed the rate of increase in percent variance explained (i.e. the ratio of between-cluster to total sum of squares) decreased markedly beyond six clusters (Table S6), cumulative variance accounted for by then being 77.03%. Accordingly, the six clusters were superimposed onto the plots of the first two axes of the ordinations (Figure 4; Figure S6). The time series of cluster assignments was also plotted, superimposed onto global ice volume as reflected by the LR04 benthic $\delta^{18}O$ stack (Figure 5). The latter figure showed cluster 1 to comprise fully glacial time slices, whereas cluster 6 included the majority of fully interglacial time slices. Superimposed onto the PCoord (NMDS) first two axes plot (Figure 4; Figure S6), cluster 1 points had the most negative (positive) axis 1 scores but a wide range of axis 2 scores, whereas cluster 6 had strongly positive (negative) axis 1 scores but (and) negative axis 2 scores. These patterns are consistent with the correlations between axis scores and principal climatic forcing variables, fully glacial cluster 1 time slices having low values of $[CO_2]_{atm}$ and large global ice volumes, but being relatively insensitive to 65° N summer insolation, whereas fully interglacial cluster 6 time slices show the opposite pattern with respect to $[CO_2]_{atm}$ and global ice volume. The negative axis 2 scores for cluster 6 time slices indicate that they tend to be associated with lower values of 65° N summer insolation. Time slices placed in cluster 5 have similarly high positive (negative) PCoord (NMDS) axis 1 scores to those of cluster 6 time slices, but positive PCoord (NMDS) axis 2 scores, indicating an association with higher values of 65° N summer insolation. Examination of Figure 5 shows time slices in cluster 5 tend to lie on the 'flanks' of glacial stages, being especially characteristic of time slices associated with glacial terminations; this is consistent with their association with higher values of 65° N summer insolation that typically reaches peak values during glacial terminations.

Time slices in clusters 4 and 3 have low negative (positive) to medium positive (negative) PCoord (NMDS) axis 1 scores (Figure 4; Figure S6), lying generally to the left (right) of those in clusters 6 and 5, respectively. Similar to clusters 6 and 5, time slices in cluster 4 generally have negative PCoord (NMDS) axis 2 scores, whereas those in cluster 3 have positive scores, indicating cluster 4 time slices

TABLE 3 Global biome pattern dissimilarity: Multiple linear regression analysis.

	Coefficient	Standard error	*t*	*p*	R^2
Constant	4.34	2.59	1.673	0.0959	–
Atmospheric CO_2 concentration (ppmv)	−0.0488	0.00399	−12.236	3.78×10^{-26}	0.825
65° N summer insolation ($W m^{-2}$)	0.0090	0.00320	2.827	0.00516	0.00962
Benthic $\delta^{18}O$ (‰)	2.3097	0.232	9.969	2.63×10^{-19}	0.782

Note: $F = 508$, df 3203, $p = 4.55\times10^{-94}$, adjusted multiple $R^2 = 0.881$.

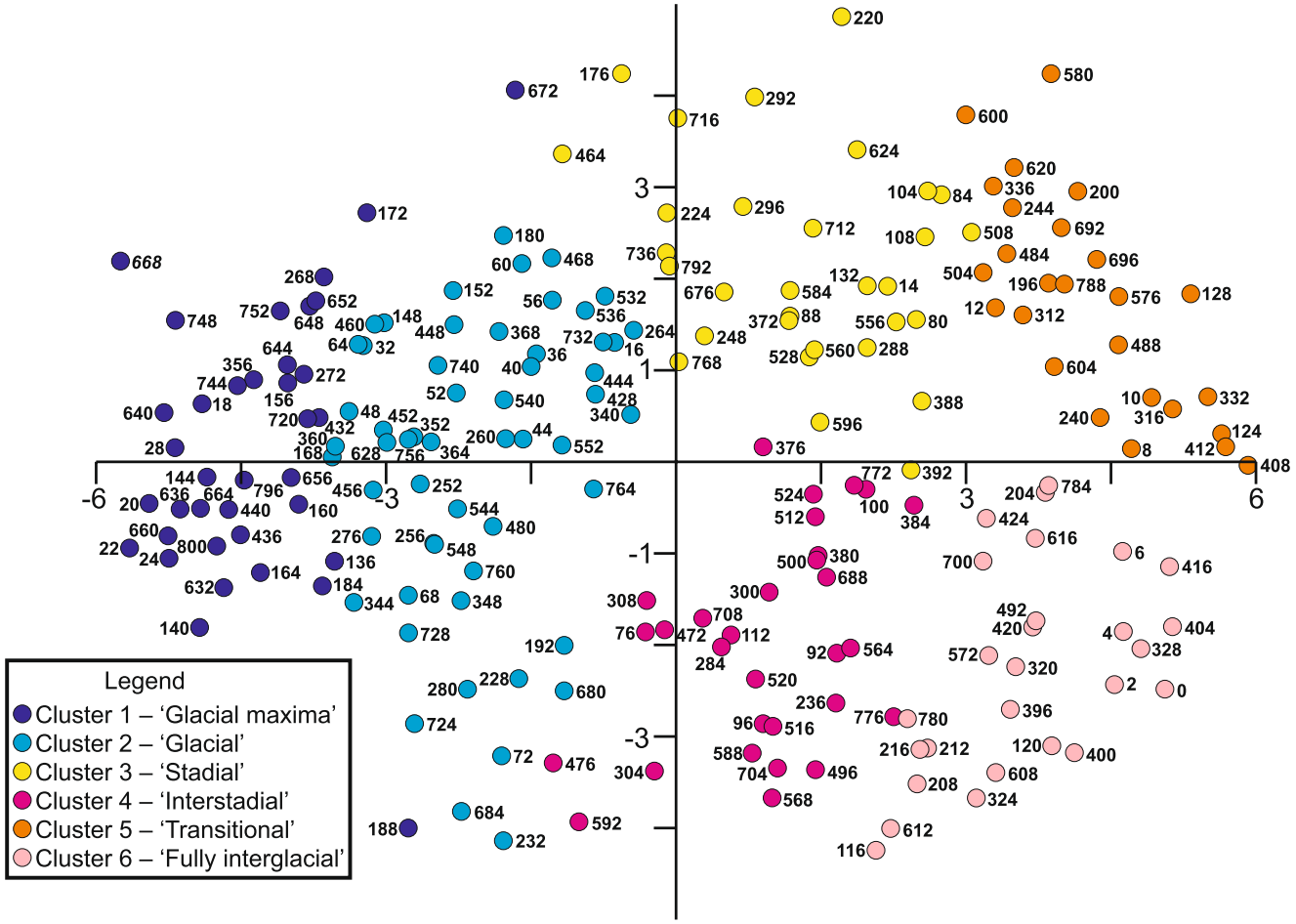

FIGURE 4 Principal coordinates analysis of global biome pattern dissimilarities. Plot of principal coordinate axis 1 (horizontal: eigenvalue 2023.5, variance accounted for 41.97%) versus axis 2 (vertical: eigenvalue 846.5, variance accounted for 17.56%). Each point represents a time slice and is labelled with its age (ka). Points are coloured to indicate to which of the six clusters, identified using *K*-means cluster analysis, they belong: cluster 1—blue; cluster 2—cyan; cluster 3—yellow; cluster 4—magenta; cluster 5—orange; cluster 6—pink.

are associated with lower and cluster 3 time slices with higher 65° N summer insolation values. Cluster 4 time slices are associated with relatively low global ice volumes typical of long-lasting interstadials (Figure 5), whereas those of cluster 3 are associated with greater ice volumes but higher 65° N summer insolation. These clusters thus in many respects parallel clusters 6 and 5, with clusters 6 and 4 associated with ice volume minima, whereas clusters 5 and 3 comprise time slices with higher northern hemisphere summer insolation values typical of the 'flanks' of ice volume minima.

The time slices of cluster 2 generally have low to moderate negative (positive) PCoord (NMDS) axis 1 scores (Figure 4; Figure S6), falling between the time slices of cluster 1, with high negative (positive) scores, and those of clusters 3 and 4. As with cluster 1, cluster 2 time slices have a wide range of axis 2 scores. They generally have

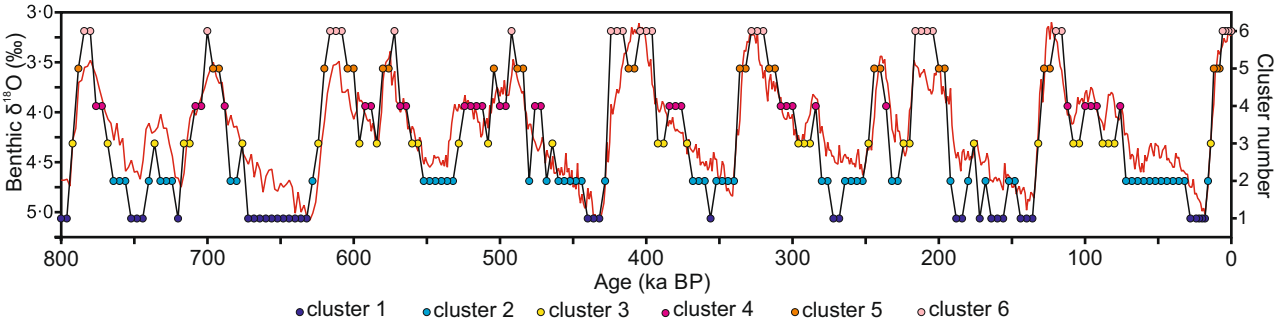

FIGURE 5 *K*-means cluster membership in relation to global ice volume. Time series of *K*-means cluster membership of time slices, each time slice being represented by a dot, coloured according to cluster membership as in Figure 4, and plotted on a vertical scale reflecting cluster number, the time slices being connected in temporal order by the thin black line. To provide context, the global ice volume, as reflected by the LR04 benthic $\delta^{18}O$ stack (Lisiecki & Raymo, 2005), is shown by the red line.

relatively high global ice volumes (Figure 5), typical of stadial, but not full glacial, conditions.

3.4 | Global biome extents and above-ground vascular plant biomass 800 ka to present

In addition to changes in location and regional extents of major biomes (Figures 1 and 2; Figures S3 and S4 and Slideshow), there are marked contrasts in the simulated historical changes in their global extents (Figure 6). Whereas most biomes show obvious changes in extent, Tropical Evergreen Forest shows only small changes in simulated global extent since 800 ka, despite its relatively high mean extent. In contrast, Temperate Shrubland, similar in mean extent to Tropical Evergreen Forest, shows moderate magnitude fluctuations corresponding to the ca. 23 ky precession cycle, peaks in biome extent generally corresponding to 65° N summer insolation minima and vice versa. Several other biomes also show extent changes principally linked to the precession cycle, albeit that some have peak extents corresponding to 65° N summer insolation maxima (e.g. Boreal Evergreen Needle-leaved Forest), others to minima (e.g. Boreal Parkland). For other biomes, dominant changes in their global extent relate to the ca. 100 ky glacial–interglacial cycle; Desert, for example, generally peaks in global extent during glacial stages, whereas Tropical Raingreen Forest reaches greatest extents during interglacials. In several cases, biomes showing similar patterns of extent changes corresponding to the glacial–interglacial cycle have contrasting patterns of change corresponding to precession cycles. Thus, both Boreal Evergreen Needle-leaved Forest and Boreal Parkland generally have greater extents during interglacials than during glacials, but show opposite responses to 65° N summer insolation maxima and minima related to the precession cycle.

Although we estimate total ice-free land area to have varied by <±3% since 800 ka (Figure 6), and Tropical Evergreen Forest, accounting for 38% of simulated total global carbon mass under present conditions, is simulated to have ranged only between 79% and 107% of its present simulated extent, simulated total global carbon mass ranges between 54% and 102% of its present simulated value (Figure 7). Whilst this large magnitude variation in total global carbon mass reflects in part reductions in temperate and boreal forest biome extents during glacials, it principally reflects a simulated reduction in carbon mass per unit area, both of individual biomes and globally, during glacials. Despite extensive continental ice sheets present during glacial stages, the associated eustatic sea level reduction results in greater total ice-free land area estimates for glacials (Figure 6), with a resulting weak negative correlation between total global carbon mass and total ice-free land area ($r = -0.211$, $p < 0.01$). Globally, simulated carbon mass per unit area, however, ranges between 53% and 102% of its present value, with a range of 73–103% for Tropical Evergreen Forest; both show strong positive correlation with $[CO_2]_{atm}$ (global: $r = 0.946$, $p << 0.001$; Tropical Evergreen Forest: $r = 0.934$, $p << 0.001$). $[CO_2]_{atm}$ is thus expected strongly to predict simulated total global carbon mass, although other factors, such as varying seasonal solar radiation intensity, are also likely to have an influence (Figure 7). Multiple linear regression of total global carbon mass, as dependent variable, upon $[CO_2]_{atm}$, 65° N summer insolation and benthic $\delta^{18}O$, as independent variables, confirmed these three variables strongly predict total global carbon mass, the first two achieving very small p values with $[CO_2]_{atm}$ the strongest individual predictor (Table 4).

3.5 | Past biome patterns and present biological diversity patterns

Previous studies have reported relationships between contemporary species richness and past biome constancy (Colville et al., 2020; Huntley et al., 2016, 2021) and have identified a relationship between tree species-richness in the temperate forests of North America, Europe and eastern Asia and glacial forest biome extents in those regions (Huntley, 1993). Our simulations quantify biome extent variations since 800 ka (Table 5; Table S7), allowing exploration of the degree to which contemporary species richness is more generally related to past biome extent variation. Some obvious parallels emerge between relative species richness and past global biome extent variation. Tree species richness (Keppel et al., 2021), for example, is

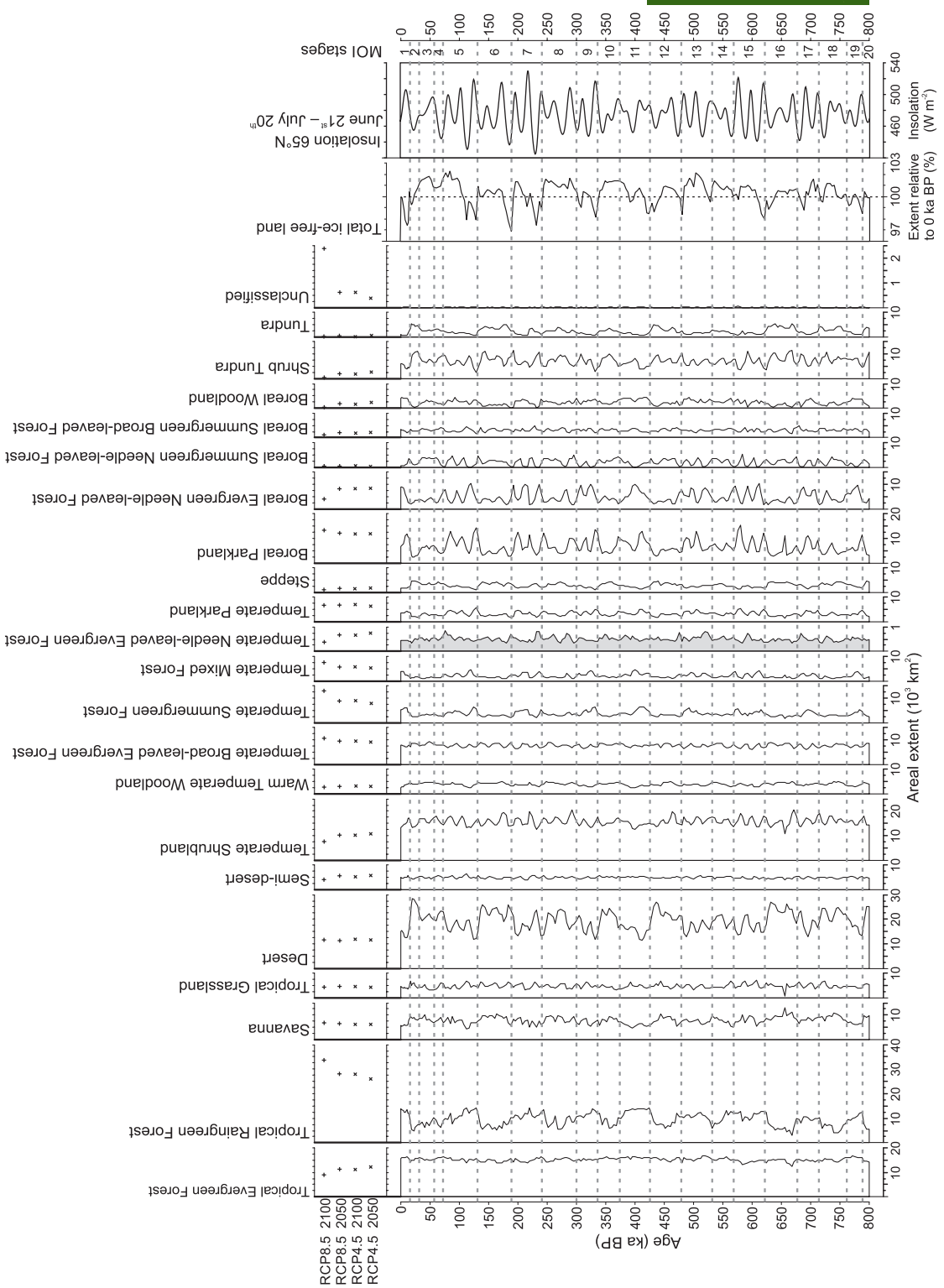

FIGURE 6 Global extents of simulated biomes. Simulated global areal extent of each biome for the series of 206 palaeoclimate time slices, 800 to 2 ka, for the present, and for projections for 2050 and 2100 under the RCP4.5 and RCP8.5 emissions pathways. The total extent of ice-free land (see Appendix S1), expressed relative to that at present, 65° N summer insolation (21 June–20 July; after Laskar et al., 2004), and marine oxygen isotope (MOI) stage boundaries (from https://lorraine-lisiecki.com/LR04_MISboundaries.txt, downloaded 9 May 2022) are also shown. RCP, representative concentration pathway. (*Note*: The horizontal scales of the shaded graphs for Temperate Needle-leaved Evergreen Forest and Unclassified differ from those of the remainder by a factor of 0.1.)

generally greatest in Tropical Evergreen Forest, mean and minimum extents of which are 96.6% and 79.1% of its present potential extent, whereas richness is less in Temperate Summergreen Forest, mean and minimum extents 67.3% and 34.5%, and less again in Boreal Evergreen Needle-leaved Forest, mean and minimum extents 53.3% and 17.5%. Although various present and past mechanisms have

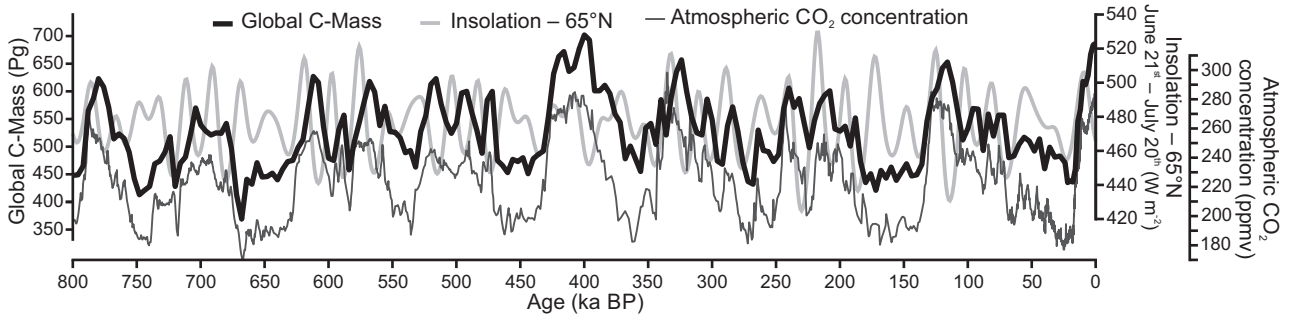

FIGURE 7 Simulated total global above-ground vascular plant biomass 800 ka to present. Total global above-ground vascular plant biomass (heavy black line) simulated by LPJ-GUESS for 206 palaeoclimate time slices and for the present. For comparison, the summer (21 June–20 July) insolation at 65° N (smooth light grey line), computed following Laskar et al. (2004), and atmospheric carbon dioxide concentration (dark grey line), following Bereiter et al. (2015; data downloaded 3 October 2019 from http://ncdc.noaa.gov/paleo/study/17975), are also shown.

TABLE 4 Global total above-ground vascular plant biomass: Multiple linear regression analysis.

	Coefficient	Standard error	*t*	*p*	R^2
Constant	368.95	62.692	5.885	1.62×10^{-8}	–
Atmospheric CO_2 concentration (ppmv)	2.2932	0.09632	23.809	1.13×10^{-60}	0.882
65° N summer insolation ($W m^{-2}$)	−0.6627	0.07746	−8.555	2.87×10^{-15}	0.00432
Benthic $\delta^{18}O$ (‰)	−10.178	5.604	−1.816	0.07079	0.6042

Note: $F=714$, df 3203, $p=1.58\times10^{-107}$, adjusted multiple $R^2=0.912$.

been hypothesised to underlie the general equator to pole diversity gradient, contrasting variations in past biome extents in three longitudinal segments, corresponding to the Americas, Europe plus Africa, and Asia plus Beringia (Table 5), and their relationships to present regional diversities, provide new insights and stronger evidence that present species richness, especially tree species richness of forest biomes, is related to past biome extent.

Temperate zone forests of eastern Asia are well known to have considerably greater tree diversity than do those of North America, that, in turn, have greater diversity than those of Europe (see e.g. Keil & Chase, 2019). This pattern is closely paralleled by past extents of Temperate Summergreen Forest and Temperate Mixed Forest in these regions. Mean (minimum) relative extents of Temperate Summergreen Forest in the three segments (Asia–Beringia, Americas, Europe–Africa) are 195.5% (75.0%), 73.0% (28.1%) and 28.1% (0.5%), whilst those for Temperate Mixed Forest are 79.2% (53.4%), 57.8% (6.7%) and 36.8% (1.9%). Furthermore, these differences in past relative extents in the three segments are much greater in magnitude than the differences in their absolute extents (Table S7). Mean simulated extents (Mm^2) of Temperate Summergreen Forest and Temperate Mixed Forest in the three segments are, respectively, 1.468 and 0.694 (Asia–Beringia), 1.411 and 0.633 (Americas), and 0.769 and 0.721 (Europe–Africa). The combined mean area of the two biomes in Europe–Africa is thus 68.9% of that in Asia–Beringia and 72.9% of that in the Americas, the difference in combined mean area between Asia–Beringia and the Americas being only 5.5%.

Tree species-richness differences are not limited to temperate forests; Tropical Evergreen Forest tree diversity is highest in the Americas, especially South America, high in south-east Asia and the islands of the Malay Archipelago, and lower in Africa (Keppel et al., 2021). Once again, this parallels past relative mean (minimum) biome extent in the three segments: 104.5% (86.1%; Americas); 90.5% (73.4%; Asia–Beringia); 82.8% (37.5%; Europe–Africa). In this case, however, there is also a more marked difference in mean absolute biome extent, with areas in the latter two bands only 32.1% and 31.8%, respectively, of that in the first.

3.6 | Potential future global biome patterns

Dissimilarities between potential present, LIG and LGM global biome patterns and those for climatic conditions projected for 2050 and 2100 under the RCP4.5 and RCP8.5 greenhouse gas concentration pathways (van Vuuren et al., 2011) reveal potential future biome pattern dissimilarities from the present and LIG similar to those for fully glacial time slices (Tables 2 and 6), and even greater dissimilarities from the LGM. Inclusion of the projected future simulations in an NMDS ordination shows the direction of change is almost diametrically opposite to that for glacial time slices (Figure 8), emphasising that projected future conditions are without parallel over the past 800 ky.

Striking changes in extent of several biomes, notably increases for Tropical Raingreen Forest and Temperate Summergreen Forest,

TABLE 5 Variation in biome extents since 800 ka relative to their present extent (%).

Biome	Global			Americas (135° W–30° W)			Europe–Africa (30° W–65° E)			Asia–Beringia (65° E–135° W)		
	Min	Mean	Max	Min	Mean	Max	Min	Mean	Max	Min	Mean	Max
Tropical Evergreen Forest	79.1	**96.6**	107.4	86.1	**104.5**	114.5	37.5	**82.8**	108.2	73.4	**90.5**	106.9
Tropical Raingreen Forest	21.7	**68.1**	101.0	29.8	**71.4**	120.8	22.1	**66.9**	109.0	5.5	**66.3**	131.1
Savanna	78.6	**137.4**	229.1	53.8	**193.0**	429.7	70.2	**134.0**	210.3	65.0	**126.3**	238.7
Tropical Grassland	13.7	**105.4**	154.8	23.4	**128.0**	360.5	2.7	**89.1**	154.8	29.3	**126.9**	215.6
Desert	74.9	**127.8**	186.6	42.9	**103.9**	163.2	82.9	**110.4**	131.0	43.1	**221.0**	467.4
Semi-desert	77.3	**99.4**	127.5	67.3	**87.4**	111.0	73.1	**93.3**	115.5	74.4	**106.4**	145.5
Temperate Shrubland	81.2	**118.0**	154.8	63.6	**97.7**	148.7	94.7	**142.0**	210.8	75.3	**103.7**	126.7
Warm Temperate Woodland	95.5	**149.5**	194.3	87.6	**125.9**	184.0	74.7	**142.8**	228.5	90.2	**206.5**	344.6
Temperate Broad-leaved Evergreen Forest	74.8	**97.2**	115.4	67.5	**100.7**	126.9	48.2	**97.0**	162.2	79.0	**93.0**	112.1
Temperate Summergreen Forest	34.5	**67.3**	120.9	28.1	**73.0**	122.0	0.5	**28.1**	111.4	75.0	**195.5**	278.1
Temperate Mixed Forest	23.0	**52.1**	114.3	6.7	**57.8**	138.0	1.9	**36.8**	111.4	53.4	**79.2**	125.4
Temperate Needle-leaved Evergreen Forest	71.8	**111.9**	188.5	34.3	**67.7**	105.4	50.4	**213.5**	536.9	69.5	**162.3**	249.9
Temperate Parkland	42.9	**92.7**	157.0	42.9	**127.7**	338.6	30.7	**83.8**	150.7	34.9	**80.1**	113.2
Steppe	58.0	**154.2**	248.3	77.9	**190.0**	262.5	100.0	**382.2**	1185.9	35.7	**125.8**	181.1
Boreal Parkland	37.1	**101.6**	233.2	19.7	**85.8**	168.2	90.9	**236.9**	599.4	15.5	**79.9**	240.5
Boreal Evergreen Needle-leaved Forest	17.5	**53.3**	113.9	5.6	**37.4**	111.2	5.1	**79.0**	188.0	24.6	**52.3**	121.1
Boreal Summergreen Needle-leaved Forest	0.0	**418.6**	1081.3	0.0	**684.7**	2406.6	—[a]	—[a]	—[a]	0.0	**338.1**	850.4
Boreal Summergreen Broad-leaved Forest	51.4	**92.9**	146.9	8.9	**40.8**	117.9	20.2	**305.3**	629.3	42.7	**101.0**	168.1
Boreal Woodland	4.8	**60.1**	112.4	0.0	**153.1**	602.3	—[a]	—[a]	—[a]	5.0	**53.8**	107.2
Shrub Tundra	38.9	**119.6**	191.5	12.1	**81.4**	169.9	34.0	**218.5**	612.6	46.6	**125.8**	200.4
Tundra	61.2	**262.7**	585.9	3.0	**105.3**	563.6	29.1	**802.6**	3968.3	78.0	**301.5**	664.2
Unvegetated	0.0	**175.7**	1744.5	0.0	**470.6**	9286.1	0.0	**140.5**	1642.2	—[a]	—[a]	—[a]

Note: Cells are shaded blue/orange where their value deviates by ±>5% from the present value. Four progressively darker shades of blue indicate values in the ranges: <95% – 70%; <70% – 50%; <50% – 30%; and <30%. Four progressively darker shades of orange indicate values in the ranges: >105% – 150%; >150% – 250%; >250% – 500%; and >500%.

[a]Zero extent simulated for present prevents calculation of past relative values.

and decreases for Tropical Evergreen Forest, Temperate Shrubland, Temperate Needle-leaved Evergreen Forest and Boreal Evergreen Needle-leaved Forest (Figure 6; Figure S7) contribute to the large dissimilarities. Although there is also an increase in unclassified grid cells, this has very limited impact because even at their maximum, in the 2100 projection under RCP8.5, they account for only 1.8% of global ice-free land area.

4 | DISCUSSION

4.1 | Global biome patterns and the paradigm hypothesis

Our results support the hypothesis that ascribes the differing spatial and temporal vegetation patterns of successive interglacials to climatic differences, these, in turn, being ultimately caused by the novel orbital forcing of each successive stage. However, multiple linear regression of biome dissimilarity relative to present upon three principal climatic forcing factors identified $[CO_2]_{atm}$ as the strongest individual predictor, followed by global ice volume, with northern hemisphere summer insolation as the weakest predictor. This result is reinforced both by the past time slice most dissimilar from the 'present' being that with the lowest $[CO_2]_{atm}$ (668 ka, 174 ppmv), and by the similar magnitude of dissimilarity for the RCP8.5 2100 simulation ($[CO_2]_{atm}$ 937 ppmv), 'present' (0 ka) $[CO_2]_{atm}$ being specified as 280 ppmv.

The important contribution to Quaternary climatic changes of variations in $[CO_2]_{atm}$ was demonstrated in a modelling study by Berger and Loutre (2000) showing that, whilst orbital forcing was the 'pacemaker' for glacial–interglacial climatic cycles, variations in $[CO_2]_{atm}$ were necessary to reproduce observed climatic changes, and in particular to generate the temperature variations and southward extensions of northern hemisphere ice sheets during glacial stages. Our results, whilst supporting the hypothesis that spatial and temporal changes in Quaternary vegetation, in particular differences in vegetation between successive interglacials, were driven by changing climatic conditions, also demonstrate a similarly important role of variations in $[CO_2]_{atm}$ in driving vegetation changes.

4.2 | Global biome extents and above-ground vascular plant biomass

The direct physiological effects upon plants (Urban, 2003), and hence vegetation, of changes in $[CO_2]_{atm}$ have received considerable attention in the context of the accelerating increase in $[CO_2]_{atm}$ over the past two centuries, and especially since the mid-twentieth century, resulting from anthropogenic activities, especially burning of fossil fuels (Keeling & Graven, 2021). These effects have also received attention from Quaternary palaeoecologists, although it is the impacts of lower $[CO_2]_{atm}$ during glacial stages that has been their principal focus. Lower $[CO_2]_{atm}$ favours C4 species relative to C3 species, leading to increased extents of C4 grasslands in at least some tropical habitats during glacial stages (Urban et al., 2015). It also favours non-woody relative to woody taxa, leading to a shift in their competitive balance, especially in semi-arid or seasonally-arid regions where wildfire is a characteristic feature of the ecosystems (Bond et al., 2003; Bond & Midgley, 2012). In addition, these effects, especially the relationship between $[CO_2]_{atm}$ and plant water use efficiency, result in biases in palaeoclimate reconstructions made from palaeovegetation data if they are not taken into account (Prentice et al., 2017). LPJ-GUESS has been shown to reproduce well both FACE experiment results (e.g. Hickler et al., 2008; Zaehle et al., 2014) and estimated vegetation productivity changes 1901–2015 (Kastner et al., 2022). However, without nitrogen limitation, the version used here may overestimate the positive response of photosynthesis to increased $[CO_2]_{atm}$ (Hickler et al., 2015). Nonetheless, photosynthesis increases almost linearly with leaf-internal CO_2 pressure over the glacial–interglacial range of $[CO_2]_{atm}$ (Gerhart & Ward, 2010; Kgope et al., 2010), whereas the CO_2 effects show increasing saturation under present and future $[CO_2]_{atm}$ (Hickler et al., 2015; Long et al., 2004). Thus, substantial plant-physiological CO_2 effects on global biome patterns are likely over the past 800 ky, especially where C4 grasses compete with C3 trees.

Our results are consistent with palaeovegetation evidence of shifting balances between C4 and C3 grasses and between woody and non-woody plants as $[CO_2]_{atm}$ varied during the mid- and late-Pleistocene. Given that LPJ-GUESS simulates the direct physiological effects of changes in $[CO_2]_{atm}$ on different PFTs, it could be argued that our results are unsurprising. However, $[CO_2]_{atm}$ is not the only

TABLE 6 Projected future potential global biome pattern dissimilarities.

Concentration pathway	Date (CE)	Biome pattern dissimilarity with respect to 'Present' 0 ka BP	LGM 18 ka BP	LIG 124 ka BP
RCP8.5	2100	12.18	17.90	12.01
	2050	8.29	15.40	8.11
RCP4.5	2100	8.20	15.30	8.08
	2050	6.91	14.52	6.83

Note: See text for details of calculation of dissimilarity values.

Abbreviations: LGM, last glacial maximum; LIG, last interglacial; RCP, representative concentration pathway.

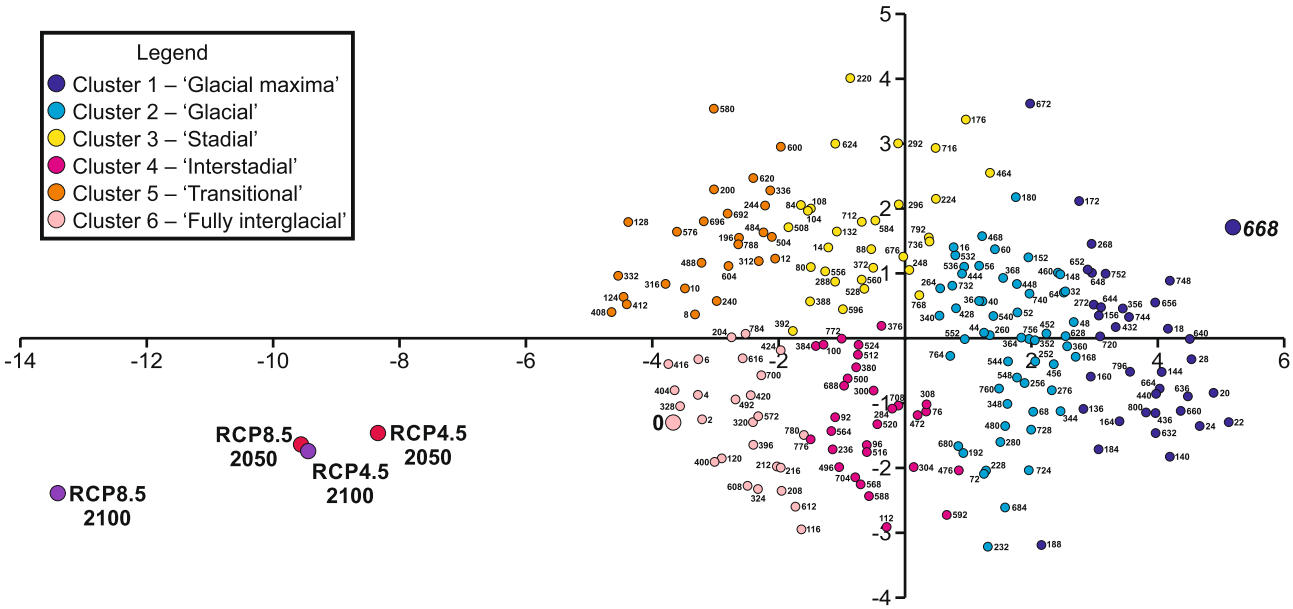

FIGURE 8 Non-metric multidimensional scaling analysis of global biome pattern dissimilarities, including projected future biome patterns. Plot of non-metric multidimensional scaling axis 1 (horizontal) versus axis 2 (vertical) for an analysis including the potential future biome patterns for 2050 and 2100 under the RCP4.5 and RCP8.5 concentration pathways, as well as all past time slices. Each point represents a time slice or potential future and is labelled with its age (ka) or concentration pathway and year (CE). Points representing past time slices are coloured to indicate to which of the six clusters, identified using *K*-means cluster analysis, they belong: cluster 1—blue; cluster 2—cyan; cluster 3—yellow; cluster 4—magenta; cluster 5—orange; cluster 6—pink. Points representing potential future biome patterns are coloured red for 2050 projections and purple for 2100 projections. RCP, representative concentration pathway.

factor influencing the simulated vegetation, climatic changes of the magnitude associated with glacial–interglacial cycles having stronger effects, especially at higher latitudes, than the $[CO_2]_{atm}$ changes.

Our results expand considerably upon the limited number of locations and time intervals for which direct palaeovegetation data are available, enabling global assessments of the changing extents of C4 grasslands and the balance between woody and non-woody PFTs. Two biomes, Savanna and Tropical Grassland, are characterised by higher LAI of the C4 grass PFT than occurs in any other biome. Savanna is simulated to have greater global extent during glacial than interglacial stages throughout the last 800 ky (Figure 6), thus inversely paralleling variation in $[CO_2]_{atm}$. Global extent of Tropical Grassland, in contrast, varies principally in relation to the precession cycle, its extent generally peaking during insolation minima, and hence when monsoons are weaker. Thus, whereas the combined extent of Savanna and Tropical Grassland is strongly negatively correlated with $[CO_2]_{atm}$ ($r = -0.726$, $p << 0.001$), the proportion of their combined extent accounted for by Tropical Grassland is strongly negatively correlated with 65° N summer insolation ($r = -0.533$, $p < 0.001$). Relationships between forest and grassland biome global extents (Table S2) and $[CO_2]_{atm}$ are even stronger. The percentage of global ice-free land area occupied by forest biomes is very strongly positively correlated with $[CO_2]_{atm}$ ($r = 0.933$, $p << 0.001$), whereas for grassland biomes the correlation is very strongly negative ($r = -0.762$, $p << 0.001$).

The substantial contribution of greater 'carbon intensity' (kg C m^{-2}) to the higher global total above-ground vegetation biomass during interglacial stages (Figure 7), when $[CO_2]_{atm}$ is greater, is an expected outcome of the CO_2-fertilisation effect upon C3 photosynthesis. Although the mechanism(s) underlying the glacial–interglacial fluctuations in $[CO_2]_{atm}$ remain the subject of debate, it is generally agreed that exchanges of CO_2 between the atmosphere and oceans play a fundamental role. Whatever the mechanism, as Prentice et al. (2011) showed in their simulations of global vegetation for the LGM and pre-industrial Holocene, glacial reduction in $[CO_2]_{atm}$ plays a fundamental role in driving the contrast between LGM and Holocene global vegetation patterns and carbon mass. Our simulations, spanning the nine glacial–interglacial cycles since 800 ka, considerably extend and reinforce this evidence.

4.3 | Past biome extents and contemporary biodiversity

Species origination through evolutionary diversification and species loss through extinction are two principal, and opposing, mechanisms contributing to determining species richness in any given region, biome or taxonomic group. Higher diversities of species will accumulate where origination rates are high and/or extinction rates are low. Varying mid- and late-Pleistocene global climate and biome patterns likely had substantial but regionally varying impacts upon both rates. Fragmentation of species' distributions during intervals when climatic conditions suitable for their persistence were available only in restricted and isolated geographical areas could potentially lead

to evolutionary divergence of the isolated populations, and hence increase species origination rate (Kadereit & Abbott, 2021). Less obviously, intervals offering suitable climatic conditions more extensively potentially allowed previously isolated but related species to exchange genetic material. Especially in the case of plants, new species can arise from such hybridisation, once again increasing species origination rate (Kadereit & Abbott, 2021).

Species extinctions can result from various mechanisms related to changing environmental conditions (Huntley, 1998). In the present context, two mechanisms are perhaps most relevant. First, species unable to track the shifting geographical location of suitable conditions are very likely to face a severely increased extinction risk. Furthermore, this risk increases the more rapidly the environment, and hence the geographical location of suitable conditions, changes. Extinction risk increase is also likely to be greater for species with more specialised habitat requirements, such as those limited to a single biome (Huntley et al., 2016). Long-term survival of such species will be greatest, and hence species richness tend to be higher, where the required habitat or biome is able to persist, notwithstanding changing environmental conditions (Colville et al., 2020; Huntley et al., 2016, 2021).

The second mechanism relates to both the widely observed species–area relationship and the increased extinction risk faced by a species if its geographical range, and hence its population, becomes restricted. Thus, according to the species–area relationship, species richness of a biome in a continental region where its mean mid- and late-Pleistocene extent was less than its present extent is expected to be less than predicted by that present extent. Species richness of the same biome in a continental region where its mean mid- and late-Pleistocene extent was similar to, or greater than, its present extent is expected to conform to, or exceed, that predicted from its present extent. In addition, extinction risk will have been higher for species associated with a biome that, in a given continental region, had a substantially reduced extent during at least one interval of the mid- and late-Pleistocene, and less for species associated with a biome that has not suffered any such severe reduction(s) in extent. Such contrasting species extinction risks likely resulted in differing rates of species loss. Hence, lower than expected species richness is predicted for biomes in continental regions where they have suffered one or more extreme reduction(s) in extent, compared to the same biome in continental regions where such extreme reduction in extent has not occurred.

Our results support the contributions to determining present species richness of the species–area relationship and mean past biome extent in different continental regions, as well as of the differential species extinction risk in biomes experiencing differing degrees of past extent reduction in different continental regions. These mechanisms are independent of species' relative capacities to shift their ranges in response to climatic changes, albeit that changes in a biome's extent in a continental region will often be associated with changes in its geographical location. This is especially the case in higher northern latitudes where biome constancy is generally low, as is species richness, contributing to the lack of any relationship between biome constancy and species richness in less diverse regions (Huntley et al., 2021). In these latitudes, a biome's past extent in a given continental region apparently has had a more marked influence on its present species richness than has its lack of areas of constancy. Nonetheless, our results also show past extent is important in regions where biomes have had substantial constancy. Tropical Evergreen Forest, for example, has large areas of high constancy (Huntley et al., 2021), but also contrasting degrees of past reduction in extent, and parallel patterns in present tree diversity, in its three principal continental regions (Keppel et al., 2021).

4.4 | Potential future global biome patterns

Since the development of global biome models, and subsequently of DGVMs, various authors have published potential future global biome pattern simulations, driven by GCM projections of future climates, and simulations of past global biome patterns, driven by GCM palaeoclimate experiments. Some previous authors have also quantified differences between simulated vegetation or biome patterns, both globally (Sykes et al., 1999; Warszawski et al., 2013) and regionally (Ni et al., 2000), for example using the Delta-V measure of biome dissimilarity developed by Sykes et al. (1999). The latter authors compared global biome patterns, simulated using BIOME 1 (Prentice et al., 1992), for the LGM (ca. 21 ka), mid-Holocene (6 ka) and LIG (P+T+ experiment, orbital forcing equivalent to 126–125 ka), based on CCM1 GCM palaeoclimate simulations (Harrison et al., 1995; Kutzbach et al., 1998), as well as for the present, and for a projected future under conditions of doubled $[CO_2]_{atm}$ relative to the pre-industrial concentration, based on OSU (Schlesinger & Zhao, 1989) and GFDL (Manabe & Wetherald, 1987) GCM climate simulations. They found the LGM simulation had the greatest dissimilarity from the present simulation, followed by the LIG and mid-Holocene simulations, with the doubled $[CO_2]_{atm}$ simulations having similar or smaller dissimilarities from the present simulation than did the mid-Holocene simulation. Whilst the LGM having the greatest dissimilarity from the present parallels our results for fully glacial time slices, their dissimilarities for doubled $[CO_2]_{atm}$ simulations contrast markedly with those we calculated for the RCP scenario simulations (Table 6) that are of comparable magnitude to those for fully glacial time slices (Table 2), albeit that their difference from the present is in the opposite direction to that of the latter time slices (Figure 8). One potential reason for this contrast is the differing $[CO_2]_{atm}$ values used in the simulations being compared. Whereas the present and doubled $[CO_2]_{atm}$ simulation pairs used by Sykes et al. (1999) used 300 and 600 ppmv (Manabe & Wetherald, 1987), and 326 and 652 ppmv (Schlesinger & Zhao, 1989), our 'present' simulation uses a pre-industrial $[CO_2]_{atm}$ of 280 ppmv, and the RCP4.5 2050 and 2100 and RCP8.5 2050 and 2100 simulations use values of 485, 538, 545 and 937 ppmv, respectively. Whilst the $[CO_2]_{atm}$ of 937 ppmv might account for extreme dissimilarities of the RCP8.5 2100 simulation (Table 6), $[CO_2]_{atm}$ used for the other projected future simulations are lower than those used in the doubled $[CO_2]_{atm}$ simulations. The

contrast in biome model formulation, however, is probably much more important than the $[CO_2]_{atm}$ values used. BIOME 1 is a static model driven only by climatic variables, whereas LPJ-GUESS is a DGVM that, in addition to simulating effects of climatic differences, simulates physiological effects on the various PFTs of differing $[CO_2]_{atm}$ values, and also the effects of changes in seasonal solar radiation intensity resulting from variation in Earth's axial obliquity. Analyses of our series of simulations show that $[CO_2]_{atm}$ has the most significant role of the three palaeoenvironmental variables we explored, both in terms of global biome pattern dissimilarities (Table 3) and total global carbon mass (Table 4). It is thus unsurprising that we simulate much more markedly differing potential future global biome patterns than did Sykes et al. (1999).

Williams et al. (2022) introduced the concept of ecocarbon sensitivity, arguing that this measure, focused upon the response of ecosystems to changes in $[CO_2]_{atm}$, enables the contentious issue of global climatic sensitivity to changes in $[CO_2]_{atm}$ to be side-stepped. Observed ecological responses to past $[CO_2]_{atm}$ changes may reflect either high ecoclimatic sensitivity and low climatic sensitivity, or vice versa, but by focusing on ecocarbon sensitivity the net ecological impact of $[CO_2]_{atm}$ changes can be explored without a need to determine climatic sensitivity. Global biome pattern dissimilarities for the present and 206 past time slices, relative to the pattern for 668 ka, the time slice with the lowest $[CO_2]_{atm}$ value, show a strong linear relationship with $\log([CO_2]_{atm})$ ($F = 1296.2$, df 1205, $p = 7.03 \times 10^{-91}$; Figure S8). However, extrapolating this past relationship to projected future $[CO_2]_{atm}$ values shows potential global biome patterns simulated for projected future $[CO_2]_{atm}$ and climatic conditions are less dissimilar than expected (Figure S8). This most probably results from the future climate experiments not taking into account more slowly responding components of the global system, including thermal inertia and mixing rate of the world's oceans, but especially ice-sheet dynamics. These 'slow' processes have inherent time scales of millennia; the Earth system thus requires millennia to reach equilibrium with changed radiative forcing, such as that being imposed by anthropogenic greenhouse gas concentration increases. Such an eventual equilibrium state is represented neither by the future climate projections we use, nor by those conventionally considered by the Intergovernmental Panel on Climate Change; instead, these projections represent a transient state of the Earth system. In contrast, an equilibrium state is approached much more closely in the palaeoclimate experiments, because the boundary conditions specified include ice-sheet extent and topography, as well as sea level, and hence the palaeogeography of continents and oceans (Singarayer & Valdes, 2010). In consequence, although our results show a significant log–linear relationship between global biome pattern dissimilarity and $[CO_2]_{atm}$ for the palaeoclimate series, this relationship does not extend to biome patterns simulated for projected future conditions.

Extrapolating the regression of global biome pattern dissimilarity, relative to the pattern for 668 ka, on $\log([CO_2]_{atm})$ to the RCP8.5 emissions scenario $[CO_2]_{atm}$ value of 937 ppmv for 2100 gives a dissimilarity value of 66.5. This approximates dissimilarities between, for example: Temperate Summergreen Forest, Temperate Mixed Forest or Temperate Needle-leaved Evergreen Forest and Tropical Evergreen Forest (61); Boreal Evergreen Needle-leaved Forest, Boreal Summergreen Needle-leaved Forest or Boreal Summergreen Broadleaved Forest and Tropical Raingreen Forest (61) or Savanna (68); or Tundra and Temperate Shrubland (62), Warm Temperate Woodland (68) or Temperate Broadleaved Evergreen Forest (62) (Table S5). Such extrapolation implies that a world that reached full equilibrium with this $[CO_2]_{atm}$ value would likely have lost most, if not all, of its polar, boreal and temperate biomes, its land surfaces being dominated by warm temperate and tropical biomes, probably with much more extensive hot deserts at lower latitudes.

5 | CONCLUSIONS

The 207 palaeovegetation and global biome simulations performed, spanning 800 ka to the present, support the hypothesis that the unique environmental conditions of successive interglacials account for the recorded palaeovegetation differences between these stages. However, analysis of the simulations shows $[CO_2]_{atm}$ plays a stronger role than northern hemisphere summer insolation in determining the vegetation differences. Furthermore, ordinations of global biome pattern dissimilarities show these two factors act to some extent independently, having correlations of the same sign with first ordination axis scores, but of opposite sign with second axis scores, and $[CO_2]_{atm}$ correlating more strongly with the first axis and northern hemisphere summer insolation with the second.

Variation in past extent differs considerably in magnitude between biomes, and also between the same biome in three longitudinal segments examined. Whilst some biomes vary in extent principally with the ca. 100 ky glacial–interglacial cycle, variation in extent of others principally follows the ca. 23 ky precession cycle. In both cases, biomes exhibit differing phase relationships and responses of opposite sign with respect to these cycles. Generally recognised differences in tree species richness between the same forest biome in different continental regions, for example, the contrasting diversity of tree genera and species between temperate forests of eastern Asia (most diverse), North America and Europe (least diverse) correspond to marked differences in past mean and minimum simulated forest biome extents in these continental regions. This supports the hypothesis that differing degrees of reduction in biome extents in different continental regions during some stages of the Middle and Late Pleistocene resulted in differing extinction risk and hence played a substantial role in generating contrasts in present diversity.

Simulated potential future global biome patterns have similar magnitudes of dissimilarity from that of the present as do simulated global biome patterns for fully glacial stages of the past 800 ky, albeit in the opposite direction in the multidimensional space of global biome pattern dissimilarity. However, whereas past global biome pattern dissimilarities exhibit a clear log-linear relationship with $[CO_2]_{atm}$, thus behaving as expected for such a global index of ecocarbon sensitivity, dissimilarity values for potential future patterns

fall well below the regression line, hence being much lower than expected given projected future $[CO_2]_{atm}$ values. Progressive increase in the degree of saturation of the CO_2 fertilisation effect upon vegetation at projected future $[CO_2]_{atm}$ values (Hickler et al., 2015; Long et al., 2004) will contribute to lesser simulated responses of global biomes to these future increases in $[CO_2]_{atm}$ than to equivalent past increases. Nonetheless, the large magnitude deviations from the regression line for future biome patterns suggest that this results principally from future climate projections taking into account only relatively faster Earth system components, and excluding slow components, in particular ice-sheet dynamics, that are likely to take millennia to reach a new equilibrium, and in doing so will lead to substantial further climatic and global biome pattern changes. Simulated potential future biome patterns, that are without any analogue during at least the past 800 ky, would have substantial negative implications for global biodiversity. The likelihood of even greater longer-term changes raises the possibility of very severe losses of global biodiversity because temperate and boreal biomes would likely be markedly reduced in extent, if not lost completely.

ACKNOWLEDGEMENTS

BH, JRMA, TH and MF were supported by Leverhulme Trust Research Grant RPG-2014-338 awarded to BH. Henk Slim and Mark Dixon provided invaluable support in relation to our use of the Durham University High Performance Computing Facility. Yvonne Collingham generated the estimates of 'present' climate for shelf grid cells and provided key support with respect to generating the climatic anomalies from HadCM3 outputs. HadCM3 simulations were performed at the Advanced Computing Research Centre of the University of Bristol http://www.bris.ac.uk/acrc/. No permits were required to carry out this research.

CONFLICT OF INTEREST STATEMENT

The authors declare no conflict of interest.

DATA AVAILABILITY STATEMENT

The following files can be accessed at https://doi.org/10.5061/dryad.pnvx0k6rw: (1) Simulated LAI and C-Mass values for all half-degree grid cells for each time slice. (2) Biome assignments for all half-degree grid cells for each time slice. (3) Extent (10^3 km^2), % of total ice-free land area, number of grid cells, % of grid cells with ice-free land, carbon mass (kg) and % of total carbon mass, for each biome for each time slice globally and for three longitudinal slices (Americas, Asia–Beringia and Europe–Africa). (4) Carbon mass (kg) and % carbon mass for each PFT and PFT aggregate for each biome. (5) The square-symmetric dissimilarity matrix for global biome patterns for the 211 simulations. (6) Total area and % ice-free land area for each half-degree grid cell for the present and 206 past time slices. (7) ArcGIS ascii grid files for a 6-min grid giving % ice cover and binary masks for ice, ocean and land for the present and 206 past time slices. (8) A .pdf slideshow of the 211 global biome maps, plus Title and Legend slides. (9) A metadata file detailing the contents and formats of the files. Code of the LPJ-GUESS version used, along with the input files, is available via Zenodo in the LPJ-GUESS community (doi: 10.5281/zenodo.7934673). Paleoclimate simulations are available from: https://www.paleo.bristol.ac.uk/ummodel/scripts/papers/Huntley_et_al_2022.html.

ORCID

Brian Huntley https://orcid.org/0000-0002-3926-2257
Ralf Ohlemüller https://orcid.org/0000-0001-9102-6481

REFERENCES

Allen, J. R. M., Forrest, M., Hickler, T., Singarayer, J. S., Valdes, P. J., & Huntley, B. (2020). Global vegetation patterns of the past 140,000 years. *Journal of Biogeography*, *47*, 2073–2090. https://doi.org/10.1111/jbi.13930

Allen, J. R. M., & Huntley, B. (2009). Last interglacial palaeovegetation, palaeoenvironments and chronology: A new record from Lago Grande di Monticchio, southern Italy. *Quaternary Science Reviews*, *28*, 1521–1538. https://doi.org/10.1016/j.quascirev.2009.02.013

Allen, J. R. M., Watts, W. A., McGee, E., & Huntley, B. (2002). Holocene environmental variability—The record from Lago Grande di Monticchio, Italy. *Quaternary International*, *88*, 69–80.

Bereiter, B., Eggleston, S., Schmitt, J., Nehrbass-Ahles, C., Stocker, T. F., Fischer, H., Kipfstuhl, S., … Chappellaz, J. (2015). Revision of the EPICA dome C CO_2 record from 800 to 600 kyr before present. *Geophysical Research Letters*, *42*, 542–549. https://doi.org/10.1002/2014gl061957

Berger, A., & Loutre, M. F. (2000). CO_2 and astronomical forcing of the late quaternary. In A. Wilson (Ed.), *The solar cycle and terrestrial climate, solar and space weather Euroconference* (pp. 155–169). Santa Cruz de Tenerife.

Bigelow, N. H., Brubaker, L. B., Edwards, M. E., Harrison, S. P., Prentice, I. C., Anderson, P. M., Andreev, A. A., Bartlein, P. J., Christensen, T. R., Cramer, W., Kaplan, J. O., Lozhkin, A. V., Matveyeva, N. V., Murray, D. F., McGuire, A. D., Razzhivin, V. Y., Ritchie, J. C., Smith, B., Walker, D. A., … Volkova, V. S. (2003). Climate change and Arctic ecosystems: 1. Vegetation changes north of 55 degrees N between the last glacial maximum, mid-Holocene, and present. *Journal of Geophysical Research-Atmospheres*, *108*, 25. https://doi.org/10.1029/2002jd002558

Bond, W. J., & Midgley, G. F. (2012). Carbon dioxide and the uneasy interactions of trees and savannah grasses. *Philosophical Transactions of the Royal Society B-Biological Sciences*, *367*, 601–612. https://doi.org/10.1098/rstb.2011.0182

Bond, W. J., Midgley, G. F., & Woodward, F. I. (2003). The importance of low atmospheric CO_2 and fire in promoting the spread of grasslands and savannas. *Global Change Biology*, *9*, 973–982.

Ciais, P., Tagliabue, A., Cuntz, M., Bopp, L., Scholze, M., Hoffmann, G., Lourantou, A., Harrison, S. P., Prentice, I. C., Kelley, D. I., Koven, C., … Piao, S. L. (2012). Large inert carbon pool in the terrestrial biosphere during the last glacial maximum. *Nature Geoscience*, *5*, 74–79. https://doi.org/10.1038/ngeo1324

Colville, J. F., Beale, C. M., Forest, F., Altwegg, R., Huntley, B., & Cowling, R. M. (2020). Plant richness, turnover and evolutionary diversity track gradients of stability and ecological opportunity in a megadiversity Centre. *Proceedings of the National Academy of Sciences of the United States of America*, *117*, 20027–20037.

Cox, P. M. (2001). *Description of the "TRIFFID" dynamic global vegetation model*. Hadley Centre technical note, 24, M.O. Hadley Centre. 16 pp.

Davies-Barnard, T., Ridgwell, A., Singarayer, J., & Valdes, P. (2017). Quantifying the influence of the terrestrial biosphere on glacial-interglacial climate dynamics. *Climate of the Past*, *13*, 1381–1401. https://doi.org/10.5194/cp-13-1381-2017

de Boer, B. (2014). *5 million year output of ice-sheet thickness, surface and bedrock elevation*. MacMillan.

de Boer, B., Lourens, L. J., & van de Wal, R. S. W. (2014). Persistent 400,000-year variability of Antarctic ice volume and the carbon cycle is revealed throughout the Plio-Pleistocene. *Nature Communications*, *5*. https://doi.org/10.1038/ncomms3999

de Boer, B., van de Wal, R. S. W., Lourens, L. J., Bintanja, R., & Reerink, T. J. (2013). A continuous simulation of global ice volume over the past 1 million years with 3-D ice-sheet models. *Climate Dynamics*, *41*, 1365–1384. https://doi.org/10.1007/s00382-012-1562-2

Forrest, M., Eronen, J. T., Utescher, T., Knorr, G., Stepanek, C., Lohmann, G., & Hickler, T. (2015). Climate-vegetation modelling and fossil plant data suggest low atmospheric CO_2 in the late Miocene. *Climate of the Past*, *11*, 1701–1732. https://doi.org/10.5194/cp-11-1701-2015

Gerhart, L. M., & Ward, J. K. (2010). Plant responses to low [CO_2] of the past. *New Phytologist*, *188*, 674–695. https://doi.org/10.1111/j.1469-8137.2010.03441.x

Gibbard, P. L., Boreham, S., Cohen, K. M., & Moscariello, A. (2005). Global chronostratigraphical correlation table for the last 2.7 million years. *Boreas*, *34*, *unpaginated*.

Hall, A. R. (1980). Late Pleistocene deposits at wing, Rutland. *Philosophical transactions of the Royal Society of London: Series B, Biological Sciences*, *289*, 135–164.

Hammer, Ø., Harper, D. A. T., & Ryan, P. D. (2001). PAST: Paleontological statistics software package for education and data analysis. *Palaeontologia Electronica*, *4*, 1–9.

Harris, I., Jones, P. D., Osborn, T. J., & Lister, D. H. (2014). Updated high-resolution grids of monthly climatic observations—The CRU TS3.10 dataset. *International Journal of Climatology*, *34*, 623–642. https://doi.org/10.1002/joc.3711

Harrison, S. P., Bartlein, P. J., Brewer, S., Prentice, I. C., Boyd, M., Hessler, I., Holmgren, K.,Izumi, K., … Willis, K. (2014). Climate model benchmarking with glacial and mid-Holocene climates. *Climate Dynamics*, *43*, 671–688. https://doi.org/10.1007/s00382-013-1922-6

Harrison, S. P., Kutzbach, J. E., Prentice, I. C., Behling, P. J., & Sykes, M. T. (1995). The response of northern-hemisphere extratropical climate and vegetation to orbitally induced changes in insolation during the last interglaciation. *Quaternary Research*, *43*, 174–184.

Haxeltine, A., & Prentice, I. C. (1996). BIOME3: An equilibrium terrestrial biosphere model based on ecophysiological constraints, resource availability and competition among plant functional types. *Global Biogeochemical Cycles*, *10*, 693–710.

Hays, J. D., Imbrie, J., & Shackleton, N. (1976). Variations in the Earth's orbit: Pacemaker of the ice ages. *Science*, *194*, 1121–1132.

Hickler, T., Rammig, A., & Werner, C. (2015). Modelling CO_2 impacts on Forest productivity. *Current Forestry Reports*, *1*, 69–80. https://doi.org/10.1007/s40725-015-0014-8

Hickler, T., Smith, B., Prentice, I. C., Mjofors, K., Miller, P., Arneth, A., & Sykes, M. T. (2008). CO2 fertilization in temperate FACE experiments not representative of boreal and tropical forests. *Global Change Biology*, *14*, 1531–1542. https://doi.org/10.1111/j.1365-2486.2008.01598.x

Hickler, T., Vohland, K., Feehan, J., Miller, P. A., Smith, B., Costa, L., Giesecke, T., Fronzek, S., Carter, T. R., Cramer, W., Kühn, I., … Sykes, M. T. (2012). Projecting the future distribution of European potential natural vegetation zones with a generalized, tree species-based dynamic vegetation model. *Global Ecology and Biogeography*, *21*, 50–63. https://doi.org/10.1111/j.1466-8238.2010.00613.x

Huntley, B. (1993). Species-richness in north-temperate zone forests. *Journal of Biogeography*, *20*, 163–180.

Huntley, B. (1998). The dynamic response of plants to environmental change and the resulting risks of extinction. In G. M. Mace, A. Balmford, & J. R. Ginsberg (Eds.), *Conservation in a changing world* (pp. 69–85). Cambridge University Press.

Huntley, B., Allen, J. R. M., Barnard, P., Collingham, Y. C., & Holliday, P. R. (2013). Species' distribution models indicate contrasting late-quaternary histories for southern and northern hemisphere bird species. *Global Ecology and Biogeography*, *22*, 277–288.

Huntley, B., Allen, J. R. M., Forrest, M., Hickler, T., Ohlemüller, R., Singarayer, J. S., & Valdes, P. J. (2021). Projected climatic changes lead to biome changes in areas of previously constant biome. *Journal of Biogeography*, *48*, 2418–2428. https://doi.org/10.1111/jbi.14213

Huntley, B., Collingham, Y. C., Singarayer, J. S., Valdes, P. J., Barnard, P., Midgley, G. F., Altwegg, R., … Ohlemüller, R. (2016). Explaining patterns of avian diversity and endemicity: Climate and biomes of southern Africa over the last 140,000 years. *Journal of Biogeography*, *43*, 874–886.

Kadereit, J. W., & Abbott, R. J. (2021). Plant speciation in the quaternary. *Plant Ecology & Diversity*, *14*, 105–142. https://doi.org/10.1080/17550874.2021.2012849

Kaplan, J. O., Bigelow, N. H., Prentice, I. C., Harrison, S. P., Bartlein, P. J., Christensen, T. R., Cramer, W., Matveyeva, N. V., McGuire, A. D., Murray, D. F., Razzhivin, V. Y., Smith, B., Walker, D. A., Anderson, P. M., Andreev, A. A., Brubaker, L. B., Edwards, M. E., … Lozhkin, A. V. (2003). Climate change and Arctic ecosystems: 2. Modeling, paleodata–model comparisons, and future projections. *Journal of Geophysical Research—Atmospheres*, *108*, 8171.

Kastner, T., Matej, S., Forrest, M., Gingrich, S., Haberl, H., Hickler, T., Krausmann, F., Lasslop, G., Niedertscheider, M., Plutzar, C., Schwarzmüller, F., Steinkamp, J., & Erb, K. H. (2022). Land use intensification increasingly drives the spatiotemporal patterns of the global human appropriation of net primary production in the last century. *Global Change Biology*, *28*, 307–322. https://doi.org/10.1111/gcb.15932

Keeling, R. F., & Graven, H. D. (2021). Insights from time series of atmospheric carbon dioxide and related tracers. *Annual Review of Environment and Resources*, *46*, 85–110. https://doi.org/10.1146/annurev-environ-012220-125406

Keil, P., & Chase, J. M. (2019). Global patterns and drivers of tree diversity integrated across a continuum of spatial grains. *Nature Ecology & Evolution*, *3*, 390–399. https://doi.org/10.1038/s41559-019-0799-0

Keppel, G., Craven, D., Weigelt, P., Smith, S. A., van der Sande, M. T., Sandel, B., Levin, S. C., Kreft, H., … Knight, T. M. (2021). Synthesizing tree biodiversity data to understand global patterns and processes of vegetation. *Journal of Vegetation Science*, *32*, e13021. https://doi.org/10.1111/jvs.13021

Kershaw, A. P., Bretherton, S. C., & van der Kaars, S. (2007). A complete pollen record of the last 230 ka from Lynch's crater, North-Eastern Australia. *Palaeogeography, Palaeoclimatology, Palaeoecology*, *251*, 23–45. https://doi.org/10.1016/j.palaeo.2007.02.015

Kgope, B. S., Bond, W. J., & Midgley, G. F. (2010). Growth responses of African savanna trees implicate atmospheric CO2 as a driver of past and current changes in savanna tree cover. *Austral Ecology*, *35*, 451–463. https://doi.org/10.1111/j.1442-9993.2009.02046.x

Kutzbach, J., Gallimore, R., Harrison, S., Behling, P., Selin, R., & Laarif, F. (1998). Climate and biome simulations for the past 21,000 years. *Quaternary Science Reviews*, *17*, 473–506.

Laskar, J., Robutel, P., Joutel, F., Gastineau, M., Correia, A. C. M., & Levrard, B. (2004). A long-term numerical solution for the insolation quantities of the earth. *Astronomy & Astrophysics*, *428*, 261–285.

Lisiecki, L. E., & Raymo, M. E. (2005). A Pliocene-Pleistocene stack of 57 globally distributed benthic $\delta^{18}O$ records. *Paleoceanography*, *20*. https://doi.org/10.1029/2004PA001071

Litwin, R. J., Adam, D. P., Frederiksen, N. O., Woolfenden, W. B., Smith, G. I., & Bischoff, J. L. (1997). An 800,000-year pollen record from Owens Lake, California; preliminary analyses. In G. I. Smith & J. L. Bischoff (Eds.), *An 800,000-year paleoclimatic record from core OL-92, Owens Lake, Southeast California* (pp. 127–142). Geological Society of America.

Long, S. P., Ainsworth, E. A., Rogers, A., & Ort, D. R. (2004). Rising atmospheric carbon dioxide: Plants face the future. *Annual Review of Plant Biology*, *55*, 591–628. https://doi.org/10.1146/annurev.arplant.55.031903.141610

Loulergue, L., Schilt, A., Spahni, R., Masson-Delmotte, V., Blunier, T., Lemieux, B., Barnola, J. M., Raynaud, D., Stocker, T. F., & Chappellaz, J. (2008). Orbital and millennial-scale features of atmospheric CH_4 over the past 800,000 years. *Nature*, *453*, 383–386. https://doi.org/10.1038/nature06950

Lüthi, D., le Floch, M., Bereiter, B., Blunier, T., Barnola, J. M., Siegenthaler, U., Raynaud, D., Jouzel, J., Fischer, H., Kawamura, K., & Stocker, T. F. (2008). High-resolution carbon dioxide concentration record 650,000–800,000 years before present. *Nature*, *453*, 379–382.

Manabe, S., & Wetherald, R. T. (1987). Large-scale changes in soil wetness induced by an increase in carbon dioxide. *Journal of Atmospheric Science*, *44*, 1211–1235.

Marchant, R., Cleef, A., Harrison, S. P., Hooghiemstra, H., Markgraf, V., van Boxel, J., Ager, T., Almeida, L., Anderson, R., Baied, C., Behling, H., Berrio, J. C., Burbridge, R., Bjorck, S., Byrne, R., Bush, M., Duivenvoorden, J., Flenley, J., De Oliveira, P., … Wille, M. (2009). Pollen-based biome reconstructions for Latin America at 0, 6000 and 18 000 radiocarbon years ago. *Climate of the Past*, *5*, 725–767.

Miller, P. A., Giesecke, T., Hickler, T., Bradshaw, R. H. W., Smith, B., Seppa, H., Valdes, P. J., … Sykes, M. T. (2008). Exploring climatic and biotic controls on Holocene vegetation change in Fennoscandia. *Journal of Ecology*, *96*, 247–259.

Miyoshi, N., Fujiki, T., & Morita, Y. (1999). Palynology of a 250-m core from Lake Biwa: A 430,000-year record of glacial-interglacial vegetation change in Japan. *Review of Palaeobotany and Palynology*, *104*, 267–283. https://doi.org/10.1016/s0034-6667(98)00058-x

Newnham, R., Alloway, B., McGlone, M., Juchnowicz, H., Rees, A., & Wilmshurst, J. (2017). A last interglacial pollen-temperature reconstruction, central North Island, New Zealand. *Quaternary Science Reviews*, *170*, 136–151. https://doi.org/10.1016/j.quascirev.2017.06.018

Ni, J., Sykes, M. T., Prentice, I. C., & Cramer, W. (2000). Modelling the vegetation of China using the process-based equilibrium terrestrial biosphere model BIOME3. *Global Ecology and Biogeography*, *9*, 463–479. https://doi.org/10.1046/j.1365-2699.2000.00206.x

Olson, J. S. (1992). World ecosystems (WE1.4). Digital raster data on a 10-minute geographic 1080 x 2160 grid. In J. J. Kineman & M. A. Ohrenschall (Eds.), *Global ecosystems database*, *version 1.0: Documentation manual*, *disc A*. National Geophysical Data Center, 254 pp.

Parrenin, F., Barnola, J. M., Beer, J., Blunier, T., Castellano, E., Chappellaz, J., Dreyfus, G., Fischer, H., Fujita, S., Jouzel, J., Kawamura, K., Lemieux-Dudon, B., Loulergue, L., Masson-Delmotte, V., Narcisi, B., Petit, J. R., Raisbeck, G., Raynaud, D., Ruth, U., … Wolff, E. (2007). The EDC3 chronology for the EPICA dome C ice core. *Climate of the Past*, *3*, 485–497.

Penkman, K. E. H., Preece, R. C., Bridgland, D. R., Keen, D. H., Meijer, T., Parfitt, S. A., White, T. S., & Collins, M. J. (2011). A chronological framework for the British quaternary based on Bithynia opercula. *Nature*, *476*, 446–449. https://doi.org/10.1038/nature10305

Petit, J. R., Jouzel, J., Raynaud, D., Barkov, N. I., Barnola, J.-M., Basile, I., Bender, M., Chappellaz, J., Davis, M., Delaygue, G., Delmotte, M., Kotlyakov, V. M., Legrand, M., Lipenkov, V. Y., Lorius, C., Pépin, L., Ritz, C., Saltzman, E., … Stievenard, M. (1999). Climate and atmospheric history of the past 420,000 years from the Vostok ice core, Antarctica. *Nature*, *399*, 429–436.

Prentice, I. C., Cleator, S. F., Huang, Y. H., Harrison, S. P., & Roulstone, I. (2017). Reconstructing ice-age palaeoclimates: Quantifying low-CO_2 effects on plants. *Global and Planetary Change*, *149*, 166–176. https://doi.org/10.1016/j.gloplacha.2016.12.012

Prentice, I. C., Cramer, W., Harrison, S. P., Leemans, R., Monserud, R. A., & Solomon, A. M. (1992). A global biome model based on plant physiology and dominance, soil properties and climate. *Journal of Biogeography*, *19*, 117–134.

Prentice, I. C., Harrison, S. P., & Bartlein, P. J. (2011). Global vegetation and terrestrial carbon cycle changes after the last ice age. *New Phytologist*, *189*, 988–998. https://doi.org/10.1111/j.1469-8137.2010.03620.x

Prentice, I. C., Jolly, D., & Biome 6000 Participants. (2000). Mid-Holocene and glacial-maximum vegetation geography of the northern continents and Africa. *Journal of Biogeography*, *27*, 507–519. https://doi.org/10.1046/j.1365-2699.2000.00425.x

R Core Team. (2021). *R: A language and environment for statistical computing*. R Foundation for Statistical Computing.

Reille, M., De Beaulieu, J. L., Svobodova, H., Andrieu-Ponel, V., & Goeury, C. (2000). Pollen analytical biostratigraphy of the last five climatic cycles from a long continental sequence from the Velay region (Massif Central, France). *Journal of Quaternary Science*, *15*, 665–685.

Schlesinger, M. E., & Zhao, Z.-C. (1989). Seasonal climatic changes induced by doubled CO_2 as simulated by the OSU atmospheric GCM/mixed-layer ocean model. *Journal of Climate*, *2*, 459–495.

Schreve, D. (2019). All is flux: The predictive power of fluctuating quaternary mammalian faunal-climate scenarios. *Philosophical transactions of the Royal Society of London: Series B, Biological Sciences*, *374*, 1–10. https://doi.org/10.1098/rstb.2019.0213

Schreve, D. C. (2001). Differentiation of the British Late Middle Pleistocene interglacials: The evidence from mammalian biostratigraphy. *Quaternary Science Reviews*, *20*, 1693–1705. https://doi.org/10.1016/S0277-3791(01)00033-6

Singarayer, J. S., & Valdes, P. J. (2010). High-latitude climate sensitivity to ice-sheet forcing over the last 120 kyr. *Quaternary Science Reviews*, *29*, 43–55.

Singh, G., Geissler, E. A., & West, R. G. (1985). Late Cainozoic history of vegetation, fire, lake levels and climate, at Lake George, New South Wales, Australia. *Philosophical transactions of the Royal Society of London: Series B, Biological Sciences*, *311*, 379–447. https://doi.org/10.1098/rstb.1985.0156

Smith, B., Prentice, I. C., & Sykes, M. T. (2001). Representation of vegetation dynamics in the modelling of terrestrial ecosystems: Comparing two contrasting approaches within European climate space. *Global Ecology and Biogeography*, *10*, 621–637.

Smith, B., Warlind, D., Arneth, A., Hickler, T., Leadley, P., Siltberg, J., & Zaehle, S. (2014). Implications of incorporating N cycling and N limitations on primary production in an individual-based dynamic vegetation model. *Biogeosciences*, *11*, 2027–2054. https://doi.org/10.5194/bg-11-2027-2014

Sykes, M. T., Prentice, I. C., & Laarif, F. (1999). Quantifying the impact of global climate change on potential natural vegetation. *Climatic Change*, *41*, 37–52.

Terrer, C., Jackson, R. B., Prentice, I. C., Keenan, T. F., Kaiser, C., Vicca, S., Fisher, J. B., Reich, P. B., Stocker, B. D., Hungate, B. A., Peñuelas, J., McCallum, I., Soudzilovskaia, N. A., Cernusak, L. A., Talhelm, A. F., Van Sundert, K., Piao, C., Newton, P. C. D., Hovenden, M. J., … Franklin, O. (2019). Nitrogen and phosphorus constrain the CO_2 fertilization of global plant biomass. *Nature Climate Change*, *9*, 684–689. https://doi.org/10.1038/s41558-019-0545-2

Torres, V., Hooghiemstra, H., Lourens, L., & Tzedakis, P. C. (2013). Astronomical tuning of long pollen records reveals the dynamic history of montane biomes and lake levels in the tropical high Andes during the quaternary. *Quaternary Science Reviews*, *63*, 59–72. https://doi.org/10.1016/j.quascirev.2012.11.004

Tzedakis, P. C. (1994). Vegetation change through glacial-interglacial cycles—a long pollen sequence perspective. *Philosophical transactions of the Royal Society of London: Series B, Biological Sciences*, *345*, 403–432.

Tzedakis, P. C., Andrieu, V., de Beaulieu, J. L., Birks, H. J. B., Crowhurst, S., Follieri, M., Hooghiemstra, H., Magri, D., Reille, M., Sadori, L., Shackleton, N. J., … Wijmstra, T. A. (2001). Establishing a terrestrial chronological framework as a basis for biostratigraphical comparisons. *Quaternary Science Reviews*, *20*, 1583–1592.

Urban, M. A., Nelson, D. M., Street-Perrott, F. A., Verschuren, D., & Hu, F. S. (2015). A late-quaternary perspective on atmospheric pCO_2, climate, and fire as drivers of C4-grass abundance. *Ecology*, *96*, 642–653. https://doi.org/10.1890/14-0209.1

Urban, O. (2003). Physiological impacts of elevated CO_2 concentration ranging from molecular to whole plant responses. *Photosynthetica*, *41*, 9–20. https://doi.org/10.1023/a:1025891825050

Valdes, P. J., Armstrong, E., Badger, M. P. S., Bradshaw, C. D., Bragg, F., Crucifix, M., Davies-Barnard, T., Day, J. J., Farnsworth, A., Gordon, C., Hopcroft, P. O., Kennedy, A. T., Lord, N. S., Lunt, D. J., Marzocchi, A., Parry, L. M., Pope, V., Roberts, W. H. G., Stone, E. J., … Williams, J. H. T. (2017). The BRIDGE HadCM3 family of climate models: HadCM3@Bristol v1.0. *Geoscientific Model Development*, *10*, 3715–3743. https://doi.org/10.5194/gmd-10-3715-2017

van Vuuren, D. P., Edmonds, J., Kainuma, M., Riahi, K., Thomson, A., Hibbard, K., Hurtt, G. C., Kram, T., Krey, V., Lamarque, J. F., Masui, T., Meinshausen, M., Nakicenovic, N., Smith, S. J., … Rose, S. K. (2011). The representative concentration pathways: An overview. *Climatic Change*, *109*, 5–31. https://doi.org/10.1007/s10584-011-0148-z

Warszawski, L., Friend, A., Ostberg, S., Frieler, K., Lucht, W., Schaphoff, S., Beerling, D., Cadule, P., Ciais, P., Clark, D. B., Kahana, R., Ito, A., Keribin, R., Kleidon, A., Lomas, M., Nishina, K., Pavlick, R., Rademacher, T. T., Buechner, M., … Schellnhuber, H. J. (2013). A multi-model analysis of risk of ecosystem shifts under climate change. *Environmental Research Letters*, *8*, 10. https://doi.org/10.1088/1748-9326/8/4/044018

Watts, W. A. (1988). Late-tertiary and Pleistocene vegetation history: Europe. In B. Huntley & T. Webb, III (Eds.), *Vegetation history* (pp. 155–192). Kluwer Academic Publishers.

Westgate, J. A., & Pearce, N. J. G. (2017). Age of some Pleistocene interglacial beds and associated fossils in eastern Beringia defined by fission tracks in glass shards of Chester Bluff tephra. *Quaternary Research*, *88*, 152–159. https://doi.org/10.1017/qua.2017.30

Williams, J. W., Huntley, B., & Seddon, A. W. R. (2022). Climate sensitivity and Ecoclimate sensitivity: Theory, usage, and past implications for the future Biospheric responses. *Current Climate Change Reports*, *8*, 1–16. https://doi.org/10.1007/s40641-022-00179-5

Zaehle, S., Medlyn, B. E., de Kauwe, M. G., Walker, A. P., Dietze, M. C., Hickler, T., Luo, Y., Wang, Y. P., el-Masri, B., Thornton, P., Jain, A., Wang, S., Warlind, D., Weng, E., Parton, W., Iversen, C. M., Gallet-Budynek, A., McCarthy, H., Finzi, A., … Norby, R. J. (2014). Evaluation of 11 terrestrial carbon-nitrogen cycle models against observations from two temperate free-air CO_2 enrichment studies. *New Phytologist*, *202*, 803–822. https://doi.org/10.1111/nph.12697

BIOSKETCH

Brian Huntley is a palaeoecologist, ecologist and biogeographer with research interests in the interactions between species, ecosystems and their changing environment. His work encompasses studies of the palaeoecology and palaeoenvironments of the Quaternary, of present ecosystems and biogeographical patterns, and of the potential impacts of anthropogenic global change on species and ecosystems. His research has considered a range of taxonomic groups, from plants to extinct Quaternary mammals, and various ecosystems, from Arctic tundra to fynbos. He has particular interest in birds and climatic change, and in the development of conservation strategies informed by research into how species and ecosystems respond to environmental changes.

Author Contributions: Brian Huntley conceived the study; Paul J. Valdes and Joy S. Singarayer performed the palaeoclimate simulations; Matthew Forrest and Thomas Hickler advised on running the palaeovegetation simulations; Matthew Forrest developed and implemented code to incorporate the climatic anomalies, extend simulations to the shelf areas and specify the varying obliquity; Matthew Forrest, Thomas Hickler and Judy R. M. Allen parameterised the PFTs; Judy R. M. Allen performed the palaeovegetation simulations and prepared Figure 6; Ralf Ohlemüller performed the non-metric multi-dimensional scaling analysis of the global biome dissimilarity matrix; Brian Huntley developed the biome inference approach and wrote the program to implement this, mapped the simulated biomes, wrote the program to generate the global biome pattern dissimilarity matrix and performed the principal coordinates and *K*-means cluster analyses of this matrix, analysed the simulation results, prepared Figures 1–5, 7 and 8, prepared the Supporting Information and drafted the manuscript. All authors commented upon and contributed to the final version of the manuscript.

SUPPORTING INFORMATION

Additional supporting information can be found online in the Supporting Information section at the end of this article.

How to cite this article: Huntley, B., Allen, J. R. M., Forrest, M., Hickler, T., Ohlemüller, R., Singarayer, J. S., & Valdes, P. J. (2023). Global biome patterns of the Middle and Late Pleistocene. *Journal of Biogeography*, *00*, 1–21. https://doi.org/10.1111/jbi.14619